JEM

Article

The Journal of Experimental Medicine

Brain endothelial TAK1 and NEMO safeguard the neurovascular unit

Dirk A. Ridder,[1]* Jan Wenzel,[1,3]* Kristin Müller,[1] Kathrin Töllner,[4,5] Xin-Kang Tong,[6] Julian C. Assmann,[1] Stijn Stroobants,[7] Tobias Weber,[1] Cristina Niturad,[1] Lisanne Fischer,[1] Beate Lembrich,[1] Hartwig Wolburg,[8] Marilyn Grand'Maison,[6] Panayiota Papadopoulos,[6] Eva Korpos,[9] Francois Truchetet,[10] Dirk Rades,[2] Lydia M. Sorokin,[9] Marc Schmidt-Supprian,[11] Barry J. Bedell,[6] Manolis Pasparakis,[12] Detlef Balschun,[7] Rudi D'Hooge,[7] Wolfgang Löscher,[4,5] Edith Hamel,[6] and Markus Schwaninger[1,3]

[1]Institute of Experimental and Clinical Pharmacology and Toxicology and [2]Department of Radiation Oncology, University of Lübeck, 23562 Lübeck, Germany
[3]German Research Centre for Cardiovascular Research (DZHK), Partner Site Hamburg/Lübeck/Kiel, 23562 Lübeck, Germany
[4]Department of Pharmacology, Toxicology, and Pharmacy, University of Veterinary Medicine Hannover, 30559 Hannover, Germany
[5]Center for Systems Neuroscience, 30559 Hannover, Germany
[6]Montreal Neurological Institute, McGill University, Montreal QC H3A 0G4, Canada
[7]Laboratory of Biological Psychology, KU Leuven, 3000 Leuven, Belgium
[8]Institute of Pathology and Neuropathology, University Hospital Tübingen, 72076 Tübingen, Germany
[9]Institute of Physiological Chemistry and Pathobiochemistry, University of Münster, 48149 Münster, Germany
[10]Service de Dermatologie, CHR Metz-Thionville, 57100 Thionville, France
[11]Department of Hematology and Oncology, Klinikum rechts der Isar, Technische Universität München, 81675 Munich, Germany
[12]Institute for Genetics, University of Cologne, 50674 Cologne, Germany

Inactivating mutations of the NF-κB essential modulator (NEMO), a key component of NF-κB signaling, cause the genetic disease incontinentia pigmenti (IP). This leads to severe neurological symptoms, but the mechanisms underlying brain involvement were unclear. Here, we show that selectively deleting *Nemo* or the upstream kinase *Tak1* in brain endothelial cells resulted in death of endothelial cells, a rarefaction of brain microvessels, cerebral hypoperfusion, a disrupted blood–brain barrier (BBB), and epileptic seizures. TAK1 and NEMO protected the BBB by activating the transcription factor NF-κB and stabilizing the tight junction protein occludin. They also prevented brain endothelial cell death in a NF-κB–independent manner by reducing oxidative damage. Our data identify crucial functions of inflammatory TAK1–NEMO signaling in protecting the brain endothelium and maintaining normal brain function, thus explaining the neurological symptoms associated with IP.

CORRESPONDENCE
Markus Schwaninger:
markus.schwaninger@pharma.uni-luebeck.de

Abbreviations used: ACh, acetylcholine; BBB, blood–brain barrier; IKK, IκB kinase complex; IP, incontinentia pigmenti; NEMO, NF-κB essential modulator; OZ, oxozeaenol; PBEC, primary brain endothelial cell; PCA, posterior cerebral artery; ROS, reactive oxygen species; TAK1, transforming growth factor β-activated kinase-1.

Cerebral blood flow and the blood–brain barrier (BBB) are essential for brain homeostasis. Both rely on an intact brain endothelium. Under normal conditions, the BBB is tightly sealed, restricting the access of blood constituents to the brain. However, during inflammatory states, the BBB may become leaky and tissue perfusion may be compromised. Indeed, inflammatory mediators, such as TNF and IL-1β, and bacterial cell wall components, such as LPS, are able to open the BBB and impair microvascular perfusion in the brain (Tsao et al., 2001; Argaw et al., 2006; Taccone et al., 2010). The capacity to open the BBB is essential for mounting an inflammatory response in the brain and may have developed during evolution to clear neurotropic viruses or other pathogens from the CNS (Roy and Hooper, 2007). Several known mechanisms increase the permeability of the BBB during inflammation involving pericytes, astrocytes, and endothelial cells (Zlokovic, 2008; Obermeier et al., 2013). However, the mechanisms that maintain and repair endothelial cell function in inflammation are still elusive. If

---

*D.A. Ridder and J. Wenzel contributed equally to this paper.

The Rockefeller University Press $30.00
J. Exp. Med. 2015 Vol. 212 No. 10 1529–1549
www.jem.org/cgi/doi/10.1084/jem.20150165

these mechanisms fail, an excessive opening of the BBB may lead to detrimental consequences, as illustrated by neurological disorders ranging from Alzheimer's disease to zoster encephalitis (Erickson and Banks, 2013). When BBB permeability is increased, extravasation of blood components interferes with normal neural function and causes epileptic seizures (Zlokovic, 2011; Obermeier et al., 2013). Even under physiological conditions, inflammatory mediators, such as TNF, IL-1β, and LPS, are present at low levels in the CNS and in the bloodstream, posing a constant challenge to the maintenance of the BBB (Boulanger, 2009; Gregor and Hotamisligil, 2011).

A central pathway in inflammation is mediated by NF-κB. By using distinct adaptor proteins, such as TRAF6 in the case of IL-1β (Lomaga et al., 1999), inflammatory mediators activate the protein kinase TAK1 (*Map3k7*; Sakurai, 2012). Subsequently, TAK1 stimulates the IκB kinase complex (IKK), which consists of the NF-κB essential modulator (NEMO; IKKγ) and the enzymatic subunits IKK1 (IKKα) and IKK2 (IKKβ; Clark et al., 2013). In turn, IKK activates the transcription factor NF-κB, which is formed by five subunits, one of them p65 (also known as RelA). In numerous diseases associated with vascular dysfunction and opening of the BBB, NF-κB signaling is activated in brain endothelial cells (Tripathi et al., 2009; Jacob et al., 2011; Kielland et al., 2012). However, at this stage, it is unclear whether endothelial NF-κB causes the vascular dysfunction or represents a protective transcriptional program in brain endothelial cells.

The genetic disease incontinentia pigmenti (IP), which is caused by inactivating mutations of the *Nemo* gene (*Ikbkg*), hints at a protective role of NF-κB signaling in the CNS. IP is named for its skin manifestations but the predominant problem is CNS involvement that often starts acutely and leads to residual deficits (Goldberg, 2004; Meuwissen and Mancini, 2012). The most frequent neurological symptoms are epileptic seizures (Meuwissen and Mancini, 2012). How *Nemo* mutations disrupt normal human brain function has been enigmatic.

To explore the mechanisms underlying the neurological symptoms of IP, we investigated mice with a germline deletion or with cell type–specific deletions of *Nemo* in the CNS. Deletion of *Nemo* in brain endothelial cells resulted in disruption of the BBB and endothelial cell dysfunction and death. Our data dissect the pathways that disturb brain endothelial function and lead to the neurological manifestations of IP when NEMO is inactivated.

RESULTS

Nemo deletion induces the death of brain endothelial cells

Female heterozygous mice with a germline deletion of the X-chromosomal *Nemo* gene ($Nemo^{-/+}$) developed skin eruptions after birth mimicking IP as has been reported previously (Makris et al., 2000; Schmidt-Supprian et al., 2000). Locomotion of $Nemo^{-/+}$ mice was slowed and they died at postnatal day (P)7–P10. To search for brain manifestations of the disease, we performed a histological evaluation of brains at P6–8. Although we did not detect any obvious pathology on hemotoxylin and eosin (H&E)– and Nissl-stained sections (not depicted), immunostainings of the endothelial cell marker CD31 and of collagen IV as an integral basement membrane component demonstrated numerous empty basement membrane strands, also known as string vessels (Brown, 2010), in the CNS of $Nemo^{-/+}$ mice (Fig. 1 A). Mice with a cell type–specific deletion of *Nemo* in neurons and glia (*Nestin-Cre;Nemo*^{Fl}, *Nemo*^{ngKO}) had no increase of string vessels, suggesting that these cell populations are not responsible for the vascular pathology (Fig. 1 B).

To delete *Nemo* selectively in brain endothelial cells, we generated a tamoxifen-inducible CreER^{T2} driver line (*Slco1c1-CreER*^{T2}) that affords selective and efficient recombination in brain endothelial cells but not in other organs (Ridder et al., 2011). Primary brain endothelial cells (PBECs) from tamoxifen-treated *Slco1c1-CreER*^{T2}*; Nemo*^{Fl} mice (*Nemo*^{beKO}) showed an ∼60% reduction in NEMO protein (Fig. 1 C) and lower NF-κB activity under basal conditions and after treatment with TNF in comparison to cells from *Nemo*^{Fl} control mice (Fig. 1, D and E). *Nemo*^{beKO} mice had numerous string vessels throughout the CNS (Fig. 1, B and F). Heterozygous deletion of *Nemo* in brain endothelial cells (*Nemo*$^{beKO/wt}$ mice) was associated with an intermediate formation of string vessels (Fig. 1 G). We found frequent string vessels in the brain of a patient who suffered from IP, confirming a similar vascular pathology in the human disease (Fig. 1 H).

Endothelial cell death has been proposed to be the main cause of string vessels (Brown, 2010). Supporting this concept, we found many brain endothelial cells in *Nemo*^{beKO} mice staining for active caspase 3, a marker of apoptotic cells (Fig. 2 A). After inducing recombination with tamoxifen, the number of apoptotic endothelial cells peaked at day 15 (Fig. 2 B), whereas the length of string vessels continuously increased even after day 15 (Fig. 2 C), demonstrating that apoptosis precedes string vessel formation and supporting the concept of a causal relationship. The angiography with sulfo-NHS-LC-biotin showed that string vessels were not perfused (Fig. 2 D). Overall, brain vessels of *Nemo*^{beKO} mice showed a normal coverage by astrocytic endfeet, pericytes, and smooth muscle cells, as well as a normal composition of the basement membrane (Fig. 2 E). However, some string vessels were apparently not covered by astrocytic endfeet and pericytes (Fig. 2, F and G, arrowheads).

Nemo deletion in brain endothelial cells disrupts the BBB and causes epileptic seizures

After inducing deletion of *Nemo* in brain endothelial cells, mice transiently lost weight in comparison to controls (Fig. 3 A) and ∼35% of those mice died (Fig. 3 B). A possible cause of the increased mortality is vasogenic brain edema, as water content in the brain was higher in *Nemo*^{beKO} mice than in *Nemo*^{Fl} controls (Fig. 3 C). In accordance with this notion, MR imaging showed that the lateral ventricles were significantly smaller in *Nemo*^{beKO} mice (6.1 ± 0.5 mm^3) than in *Nemo*^{Fl} controls (8.3 ± 0.3 mm^3; $P < 0.05$ Student's *t* test; Fig. 3 D).

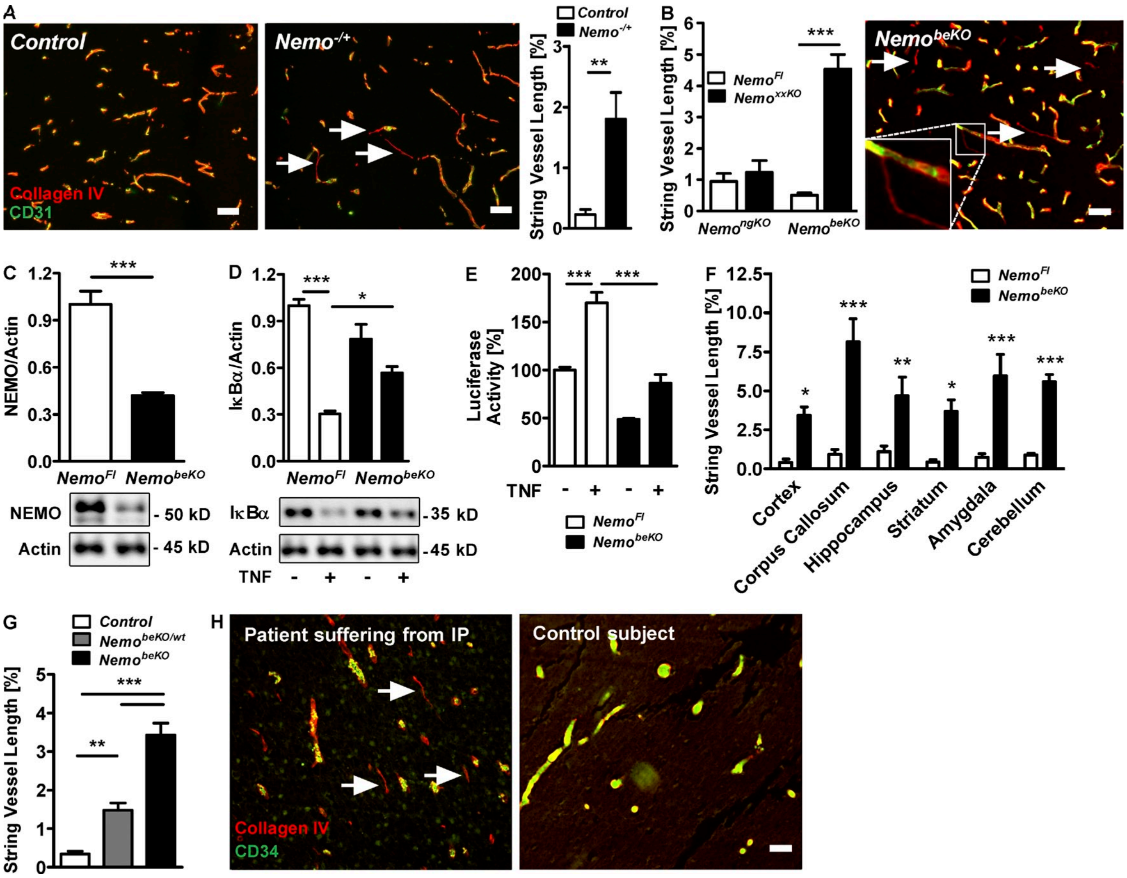

Figure 1. Deletion of *Nemo* in brain endothelial cells causes string vessel formation. (A) Representative immunostainings demonstrating string vessels (arrows) in a *Nemo*$^{-/+}$ mouse but not in a control mouse at P8. String vessels were identified as capillaries that have lost CD31-positive endothelial cells and only consist of the basement membrane protein collagen IV. (right) Quantification of string vessels in cortex at P6–8 as percentage of total vessel lengths. (B) String vessel quantification in *Nemo*^{ngKO} mice that are deficient of *Nemo* in neurons and glial cells, *Nemo*^{beKO} mice that are deficient of *Nemo* in brain endothelial cells, and *Nemo*^{Fl} controls. (right) Representative immunofluorescent staining showing string vessels (arrows) in a *Nemo*^{beKO} mouse. (inset) High magnification of a string vessel. (C) Quantification of NEMO by Western blotting in PBECs of *Nemo*^{beKO} and *Nemo*^{Fl} control mice. (D) Quantification of IκBα by Western blotting of PBECs from *Nemo*^{beKO} mice upon treatment with murine TNF (10 ng/ml). (E) NF-κB activity as determined by luciferase reporter assays in PBECs of *Nemo*^{Fl} and *Nemo*^{beKO} mice. PBECs were treated with murine TNF for 4 h before monitoring luciferase activity. (F) Distribution of string vessels in various brain areas of *Nemo*^{beKO} and *Nemo*^{Fl} mice. (G) Quantification of string vessel lengths in mice with no, heterozygous, or homozygous deletion of *Nemo* in brain endothelial cells. (H) Representative immunofluorescent staining for collagen IV and CD34 revealing string vessels (arrows) in the cortex of a patient suffering from IP (left), but not in the cortex of an age-matched subject dying from an unrelated disease (right). For further description of the IP patient, refer to (Bachevalier et al., 2003). Data are shown as means ± SEM ($n = 5$–8). *, $P < 0.05$; **, $P < 0.01$; ***, $P < 0.001$, determined by Student´s *t* test (A-C), two-way ANOVA with Bonferroni´s post test (D-F), or one-way ANOVA with Tukey's post test (G). Mice were investigated 15–18 d after start of tamoxifen treatment (B and F–G). Bars, 50 µm.

A dramatic increase in albumin and Ig levels in whole-brain extracts of *Nemo*^{beKO} mice confirmed that the BBB was damaged (Fig. 3 E). Ig extravasation occurred in all brain areas (Fig. 3 F) and increased significantly starting at day 10 after tamoxifen induction (Fig. 3, G and H), preceding the increase in brain weight at day 15 (Fig. 3 I). Staining revealed Ig localization, mainly in the parenchyma of the tissue (Fig. 3 H). The loosening of the BBB of *Nemo*^{beKO} mice was not size-selective, as intravenously injected fluorescent tracers of various sizes, ranging from 4 to 2,000 kD, were detected in higher concentrations in brain extracts of *Nemo*^{beKO} mice than of control animals (Fig. 3 J). However, we found no hemorrhages in *Nemo*^{beKO} brains on H&E stains (unpublished data). The inspection of brain sections of *Nemo*^{beKO} and control mice injected with 2,000 kD dextran demonstrated large parts of 2,000 kD dextran outside of CD31-positive endothelial cells in the perivascular space, suggesting that the majority of NEMO-deficient vessels were leaky (Fig. 3 K). In NEMO-deficient mice, vessels permeable for dextrans outnumbered the active caspase 3–positive vessels, and most leaky vessels did not show active caspase 3 staining (Fig. 3 L, arrows) implying that the death of endothelial cells is not the main cause of BBB disruption.

Vasogenic brain edema can be lethal by compressing the brain stem, a condition that leads to an altered reactivity of

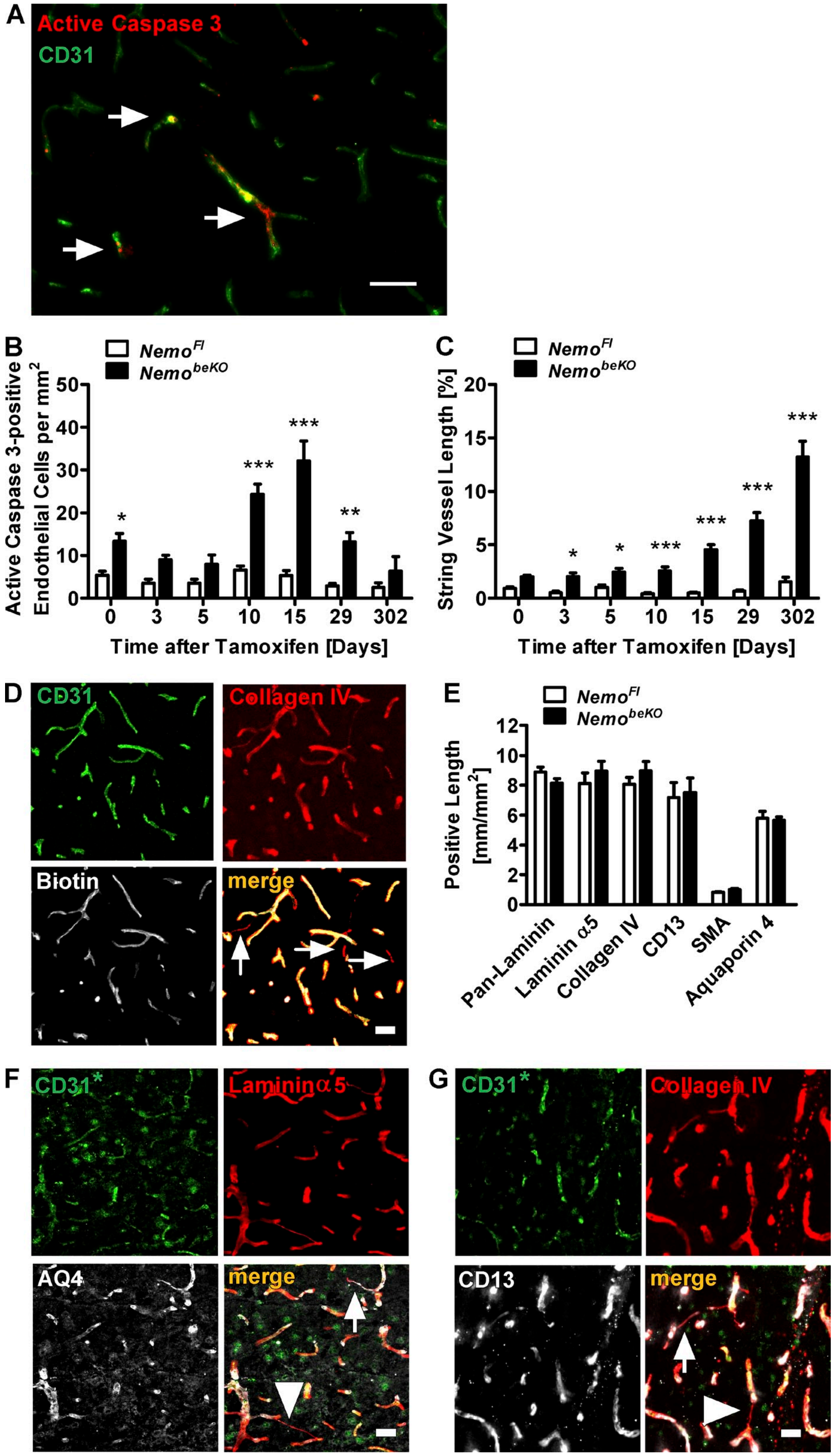

Figure 2. Deletion of *Nemo* in brain endothelial cells causes brain endothelial cell death. (A) Representative immunostaining for active caspase 3 (arrows) in the cortex of a *Nemo*^{beKO} mouse. (B and C) Quantification of active caspase 3–positive endothelial cells (B) and string vessels (C) at seven time points before and after the start of tamoxifen treatment. The difference in active caspase 3–positive cells and string vessel length between *Nemo*^{beKO} and *Nemo*^{Fl} mice before tamoxifen induction (day 0) is due to a low recombination rate in the *Slco1c1-CreER*^{T2} driver line without tamoxifen treatment (not depicted). (D) Staining of brain sections for i.v.-injected sulfo-NHS-LC-biotin to detect perfused vessels. String vessels are indicated (arrows). (E) Quantification of vessel lengths immunostained for basement membrane components (pan-laminin, laminin α5, and collagen IV), as well as pericyte (CD13), smooth muscle cell (SMA), or astrocytic endfeet markers (aquaporin 4). (F and G) Representative immunofluorescent stainings for aquaporin 4 (AQ4; F) and CD13 (G). String vessels covered by astrocytic endfeet and pericytes are indicated by arrows, while string vessels not covered are indicated by arrowheads. For the staining depicted in F and G, goat anti-CD31 antibodies had to be used (CD31*), leading to more unspecific staining. Data are shown as means ± SEM (n = 5–8). *, $P < 0.05$; **, $P < 0.01$; ***, $P < 0.001$, determined by two-way ANOVA with Bonferroni´s post test (B and C). Mice were investigated 15 d after start of tamoxifen treatment (A and D–G). Bars, 50 µm.

pupils in humans and mice (Matullo et al., 2010). However, pupillary reactivity was normal in *Nemo*^{beKO} mice (Fig. 3 M), arguing against brain stem compression as a cause of the increased mortality.

The extravasation of albumin has been reported to activate astrocytes (Obermeier et al., 2013). We found increased GFAP staining, a sign of astrocytic activation, in *Nemo*^{beKO} mice (Fig. 3 N). Because BBB dysfunction and astrocytic

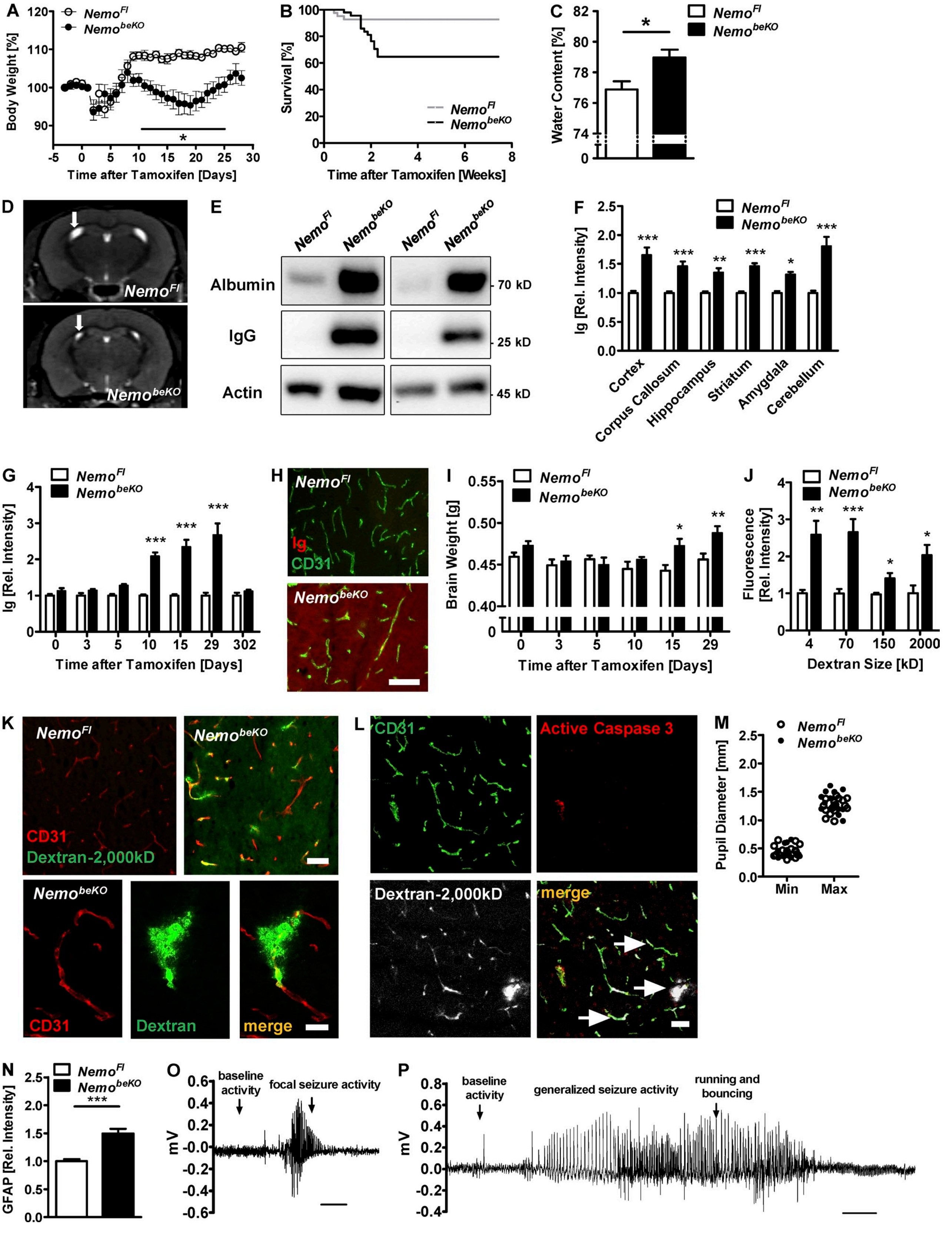

Figure 3. Deletion of *Nemo* in brain endothelial cells disrupts the BBB and causes epileptic seizures. (A) Body weight of *Nemo*^{beKO} and *Nemo*^{Fl} mice was measured before and after induction of recombination by tamoxifen (day 0). Values are presented as percentage of the body weight at day 0

activation can trigger epileptic seizures, we monitored *Nemo*^{beKO} and control mice for seizures by combined EEG/video recording. 10 out of 12 *Nemo*^{beKO} animals, but none of the 13 control mice, displayed epileptic seizure activity ($P < 0.0001$, Fisher's exact test). 3 out of 12 mice had periods of short focal seizure activity (<10 s duration; Fig. 3 O), and 7 out of 12 mice suffered from generalized epileptic seizures of >10 s duration (Fig. 3 P). Two of the *Nemo*^{beKO} mice died during seizures, suggesting that epilepsy is a cause of the increased mortality.

Nemo deletion in brain endothelial cells compromises cerebrovascular reactivity, basal cerebral blood flow, and neurovascular coupling

In *Slco1c1-CreER*^{T2} mice, recombination occurs in endothelial cells of small and large diameter vessels of the brain (Fig. 4 A). Therefore, we investigated whether deletion of *Nemo* also affects cerebrovascular reactivity. Instead of dilating in response to acetylcholine (ACh; Zhang et al., 2013), posterior cerebral arteries (PCAs) isolated from *Nemo*^{beKO} mice weakly constricted (Fig. 4 B). In contrast, vessels responded normally to the NO donor sodium nitroprusside (SNP; Fig. 4 C), the potent vasoconstrictor endothelin-1 (ET-1; Fig. 4 D), and the NO synthase inhibitor L-NNA (Fig. 4 E; Tong et al., 2012; Zhang et al., 2013), demonstrating that smooth muscle function and basal NO production were intact but endothelial-mediated relaxation was impaired.

The rarefaction of capillaries and impaired cerebrovascular reactivity in *Nemo*^{beKO} mice may affect cerebral blood flow. Indeed, arterial spin labeling (ASL) perfusion MRI revealed a significantly reduced resting blood flow throughout the CNS of *Nemo*^{beKO} mice when compared with *Nemo*^{Fl} mice (Fig. 4, F and G). Furthermore, the blood flow increase in response to whisker stimulation of *Nemo*^{beKO} mice was impaired (Fig. 4, H and I). The reduced hyperemia was not explained by structural or functional changes of neurons as whisker pad stimulation evoked similar local field potentials in the barrel cortex of *Nemo*^{beKO} and *Nemo*^{Fl} mice (Fig. 4, J–L). Moreover, we found no signs of neuronal cell death or loss of synapses in brains of *Nemo*^{beKO} mice (unpublished data). These data demonstrate that NEMO signaling in brain endothelial cells ensures normal basal perfusion and neurovascular coupling.

Nemo deletion in brain endothelial cells has behavioral consequences

To analyze whether disruption of the BBB and reduced blood flow translate into functional consequences, we performed behavioral tests. *Nemo*^{beKO} mice displayed intact contextual fear conditioning, reflecting normal learning and memory (Fig. 5 A). However, *Nemo*^{beKO} mice showed generally increased freezing during cued fear conditioning independent of the presence of the cue, although freezing behavior during the habituation phase, fear conditioning, and the context fear testing was normal, which may relate to increased state anxiety and/or overgeneralization of the fear response. Increased state anxiety is indeed consistent with two other observations. First, *Nemo*^{beKO} mice spent less time in the inner zone of the open field than *Nemo*^{Fl} mice when the vascular pathology had developed (Fig. 5 B). Second, there was a trend that *Nemo*^{beKO} mice spent less time in the open arms of the elevated plus maze than *Nemo*^{Fl} animals (Fig. 5 C), whereas their overall locomotion was unaffected (Fig. 5 D). In addition to elevated anxiety, *Nemo*^{beKO} mice showed less social behavior in the sociability test, as demonstrated by a significantly lower relative number of approaches to and relative time in the proximity of another mouse (Fig. 5 E).

TRAF6, TAK1, NEMO, and NF-κB p65 differentially regulate brain endothelial function and survival

NEMO is an essential component of the canonical pathway activating NF-κB. To explore the role of this pathway in brain endothelial cells, we deleted the upstream adaptor protein TRAF6 and the upstream kinase TAK1, as well as the p65 subunit of NF-κB, by crossing the *Slco1c1-CreER*^{T2} strain with mice carrying loxP-flanked *Traf6*, *Tak1*, or *p65* alleles and induced recombination by injecting tamoxifen (*Traf6*^{beKO}, *Tak1*^{beKO}, or *p65*^{beKO}). Western blotting revealed that *Traf6*, *p65*

($n = 7–8$). (B) Survival curves of *Nemo*^{beKO} and control mice ($n = 41–46$) after treatment with tamoxifen are shown. $P < 0.01$ (log-rank test). (C) Water content in brains of *Nemo*^{beKO} mice compared with control animals ($n = 3–5$). (D) Representative coronal anatomical MRI scans of a *Nemo*^{beKO} and a *Nemo*^{Fl} control mouse. Arrows indicate the lateral ventricles. (E) Determination of IgG brain levels by Western blotting. (F) Quantification of Ig immunostaining in various brain areas of *Nemo*^{Fl} and *Nemo*^{beKO} mice ($n = 7–8$). (G) Quantification of Ig immunostaining in the cortex at seven time points before and after the start of tamoxifen treatment ($n = 7–8$). (H) Representative images of immunofluorescent Ig detection co-stained with CD31 in the cortex at day 29 after tamoxifen treatment. (I) Brain weights at six time points before and after tamoxifen treatment. (J) Concentrations of fluorescently labeled dextrans of various molecular sizes in brain lysates after i.v. injections ($n = 7–8$). Fluorescence intensity in tissue extracts is expressed relative to *Nemo*^{Fl} controls. (K) Imaging of fluorescent 2,000-kD dextran in brain slices of *Nemo*^{Fl} and *Nemo*^{beKO} mice after staining of endothelial cells with anti-CD31. Dextran was i.v. injected. (L) Representative image of fluorescent 2,000-kD dextran in a *Nemo*^{beKO} brain slice after staining with anti-CD31 and anti-active caspase 3. Arrows, vessels negative for active caspase 3 staining. (M) Pupillary diameters were video-recorded while increasing the illumination rapidly from 1 lux (Max) to 500 lux (Min). Each dot represents the mean of two measurements for one mouse. (N) Quantification of GFAP staining in the cortex of *Nemo*^{beKO} mice and control animals. (O) Representative EEG trace of a focal seizure recorded by cortex screws above the hippocampus of a *Nemo*^{beKO} mouse. The seizure was accompanied by unspecific movement at the same place followed by a stretching of the body. (P) Representative EEG trace of a generalized seizure recorded by fronto-parietal cortex screws in a *Nemo*^{beKO} mouse. The seizure was accompanied by forelimb clonus, rearing, and loss of balance with running and bouncing. Data are shown as means ± SEM. *, $P < 0.05$; **, $P < 0.01$; ***, $P < 0.001$, determined by Student's *t* test (C and N), and two-way ANOVA with Bonferroni's post test (F, G, I, and J). Mice were investigated 19–22 d (C) or 11–16 d (D, F, and J–P) after start of tamoxifen treatment. Bars, 50 µm (H, L, K, top); 10 µm (K, bottom); and 5 s (O and P).

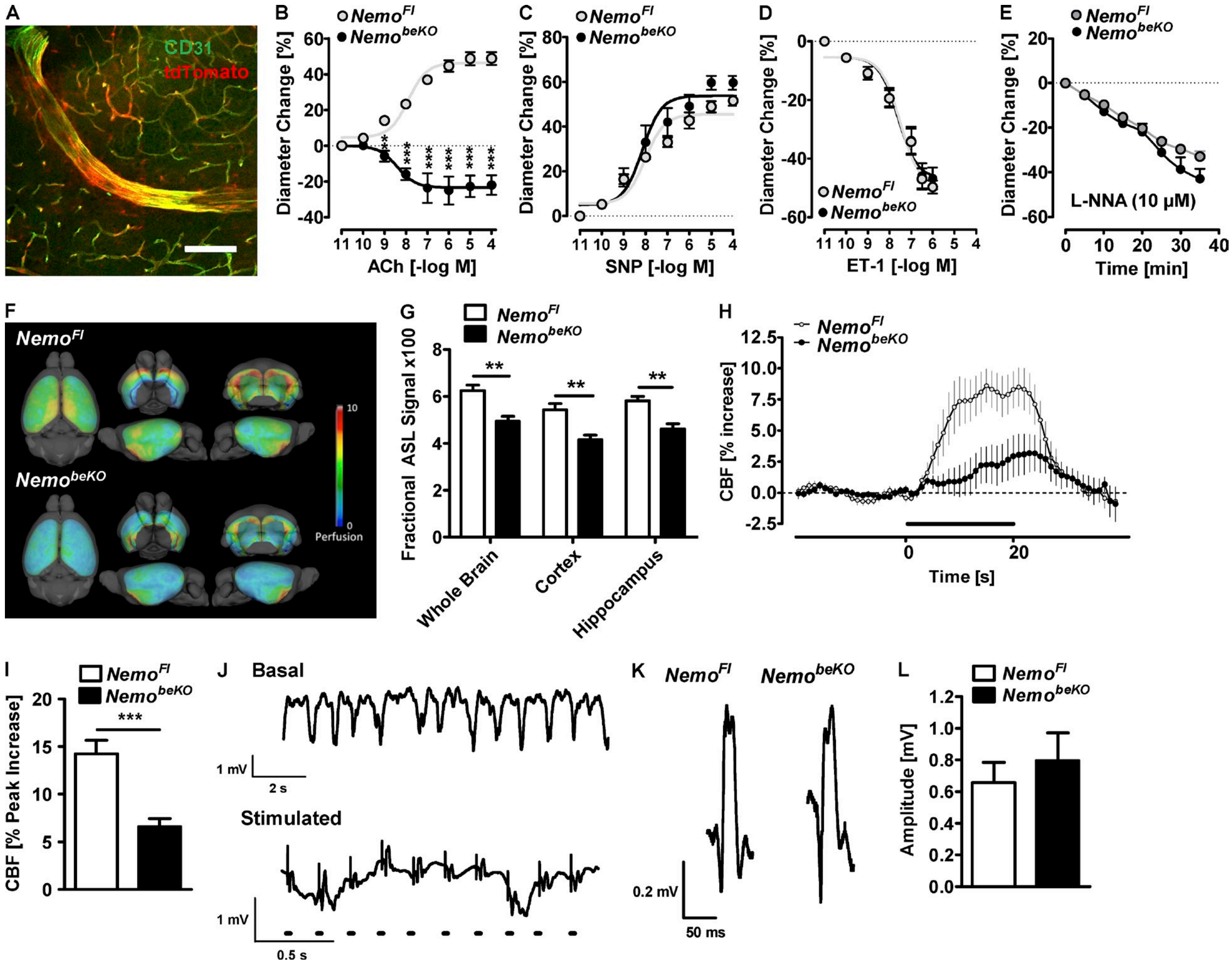

Figure 4. Deletion of *Nemo* in brain endothelial cells disturbs cerebrovascular reactivity and reduces basal cerebral blood flow and neurovascular coupling. (A) tdTomato expression after recombination in small and large CD31-positive vessels throughout the CNS of *Slco1c1-CreER*^{T2}*;Ai14* mice. A representative picture from the cortex is shown. Bar, 120 µm. (B–E) Responses of PCA segments of *Nemo*^{beKO} and *Nemo*^{Fl} mice to Ach (B), the NO donor sodium nitroprusside (SNP; C) endothelin-1 (ET-1; D), and the NO synthase inhibitor *N*ω-nitro-L-arginine, L-NNA; E) are shown (n = 4–7). (F) Cerebral perfusion as depicted by surface-projected, group-averaged ASL-MRI maps (n = 12–13). (G) Quantification of ASL-MRI tissue perfusion in three brain areas of *Nemo*^{beKO} and *Nemo*^{Fl} mice (n = 12–13). (H and I) Cerebral blood flow (CBF) responses in the somatosensory cortex of *Nemo*^{beKO} and *Nemo*^{Fl} mice evoked by whisker stimulation are shown (n = 6–7). The bar indicates stimulation. (J) Local field potentials were recorded in the somatosensory barrel cortex representing the contralateral whisker pad. (top) Basal neuronal activity. (bottom) Responses upon electrical stimulation of the whisker pad. Dots indicate stimulation. Note the different time scale for top and bottom parts. (K) Representative local field potentials of *Nemo*^{beKO} and *Nemo*^{Fl} mice are shown. (L) Quantification of the amplitude of the local field potentials. Data are shown as means ± SEM. **, $P < 0.01$; ***, $P < 0.001$, determined by repeated measures ANOVA with Bonferroni's post test (B) and Student's *t* test with Bonferroni correction (G and I). Mice were investigated 14–24 d after start of tamoxifen treatment.

(Fig. 5, F and G), and *Tak1* (Ridder et al., 2011) had been efficiently deleted in PBECs from mice of the different genotypes. Deletion of *p65* in brain endothelial cells reduced basal and TNF-stimulated NF-κB activity (Fig. 5 H) and the expression of p65 in cortical vessels (Fig. 5 I).

Brain weight, as an indicator of brain edema, and brain Ig levels were not altered by deletion of *Traf6* in brain endothelial cells (Fig. 6, A and B). However, both parameters were elevated in *Tak1*^{beKO} mice just as in *Nemo*^{beKO} animals (Fig. 6, A and B). In *p65*^{beKO} mice, we found no change of brain weight and a smaller increase in Ig staining than in *Nemo*^{beKO} and *Tak1*^{beKO} animals (Fig. 6, A and B). These findings suggest that in brain endothelial cells TAK1 activates IKK and, subsequently, the NF-κB subunit p65 to maintain the BBB. The presence of other NF-κB subunits that are able to compensate for the absence of p65 likely explains why *p65* deletion had a less pronounced effect on Ig extravasation than *Nemo* deletion and had no effect on brain weight. The TAK1–IKK–NF-κB pathway sealing the BBB appears to be independent of TRAF6, excluding upstream stimuli known to exert their effects via TRAF6, e.g., IL-1β (Lomaga et al., 1999).

By measuring the length of string vessels, we found a marked increase in *Tak1*^{beKO} and *Nemo*^{beKO} mice, but not in *Traf6*^{beKO} and *p65*^{beKO} animals (Fig. 6 C). Conversely, the length of intact

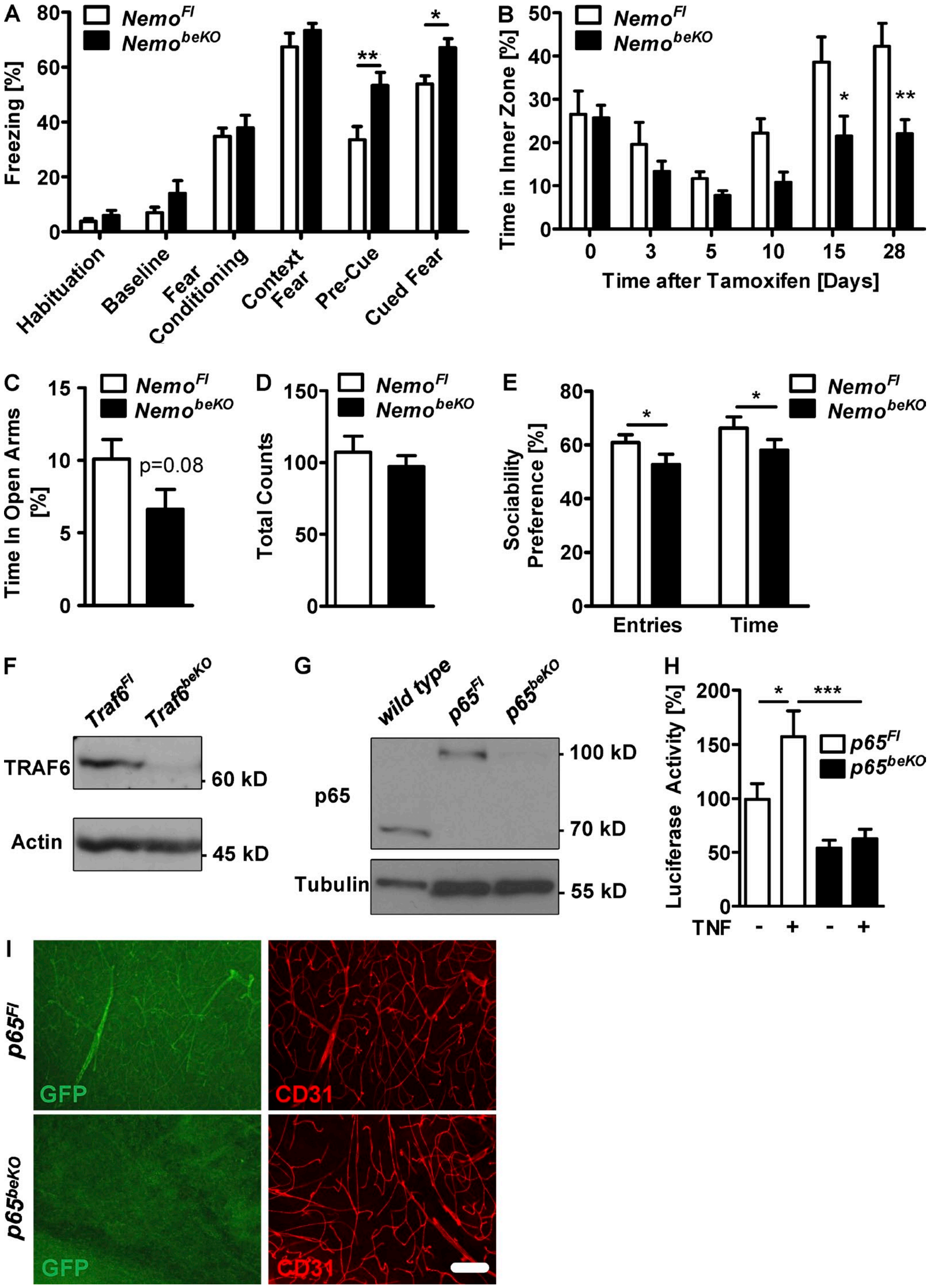

Figure 5. Deletion of *Nemo* in brain endothelial cells leads to more anxiety-related behavior and less sociability in mice. (A) Quantification of the relative freezing time in the different parts of the contextual fear conditioning test is shown (*n* = 13–18). (B) The open field test was performed at 7 time points before and after the start of tamoxifen treatment (*n* = 7–8). Injection of tamoxifen during the first 5 d led to a decreased time in the inner zone in both genotypes. (C and D) The time spent in the open arms of an elevated plus maze test is shown (C), as well as the overall activity (D) measured by total counts of entries (*n* = 13–18). (E) Sociability was tested by measuring the relative number of approaches and time spent in proximity of a conspecific in *Nemo*^{beKO} and *Nemo*^{Fl} mice (*n* = 13–18). (F) TRAF6 was measured by Western blotting of PBECs from *Traf6*^{beKO} and *Traf6*^{Fl} control mice. (G) The amount of NF-κB p65 was determined by Western blotting of PBECs from wild-type mice, *p65*^{beKO} and *p65*^{Fl} control mice. Note that endogenous p65 is replaced by a p65-eGFP fusion protein in *p65*^{Fl} PBECs resulting in a higher molecular weight when compared with wild-type PBECs. (H) NF-κB activity as determined by luciferase reporter assays in PBECs of *p65*^{Fl} and *p65*^{beKO} mice. PBECs were treated with murine TNF (10 ng/ml) or solvent for 4 h before monitoring luciferase activity (*n* = 5–6). (I) Immunostainings against GFP and CD31 of *p65*^{beKO} and *p65*^{Fl} mice are shown. To detect the GFP signal in

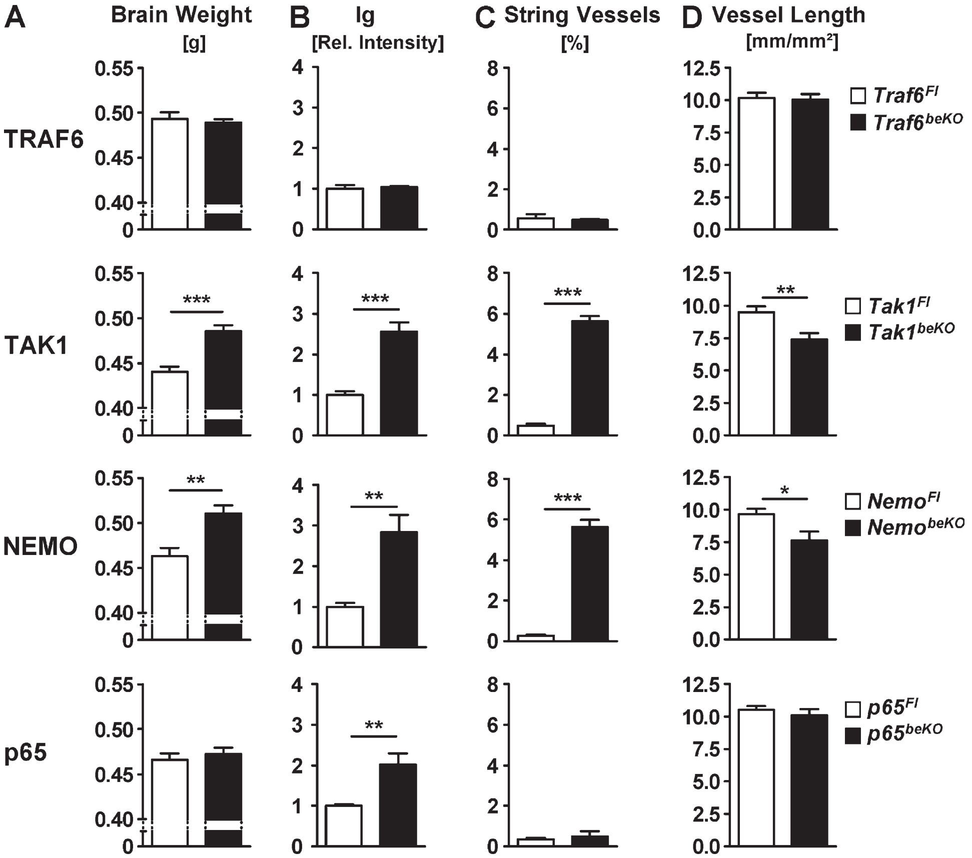

Figure 6. Brain endothelial deletion of the upstream kinase *Tak1* but not of the adaptor protein *Traf6* phenocopies *Nemo* knockout. Downstream of NEMO, NF-κB p65 regulates BBB permeability but not endothelial survival. (A) Brain weights of mice lacking different parts of the NF-κB signaling cascade in brain endothelial cells are shown. (B) Quantifications of immunofluorescent stainings of Ig in the cortex of *Traf6*^{beKO}, *Tak1*^{beKO}, *Nemo*^{beKO}, *p65*^{beKO}, and respective control mice. (C) String vessel lengths are quantified in the brains of the different mouse lines. (D) Quantifications of the total CD31-positive vessel lengths in the cortex. Data are shown as means ± SEM (n = 3–8 mice per genotype). *, $P < 0.05$; **, $P < 0.01$; ***, $P < 0.001$, determined by Student´s *t* test. Mice were investigated 15–16 d after the start of tamoxifen treatment.

CD31-stained vessels was shorter in *Tak1*^{beKO} and *Nemo*^{beKO} mice but not in *Traf6*^{beKO} and *p65*^{beKO} animals (Fig. 6 D), confirming that the appearance of string vessels reflects a loss of capillary endothelium. In summary, deletion of *Tak1* and *Nemo* led to a loss of brain vessels. Whereas the absence of p65 did not trigger endothelial cell death, it still caused increased BBB leakage, arguing for two independent mechanisms and confirming the observation that leakiness can occur in the absence of endothelial cell death (Fig. 3 L). The lack of a phenotype in *Traf6*^{beKO} mice excludes an unspecific effect of the CreER^{T2} itself.

TAK1–NEMO–IKK2 signaling regulates BBB permeability, but not brain endothelial survival

To verify that the increased brain weight and the Ig extravasation in the brain of *Tak1*^{beKO} mice reflect a disruption of the BBB, we measured the water content and the BBB permeability by intravenously injecting the tracer sodium fluorescein. In *Tak1*^{beKO} mice, the water content and the BBB permeability to fluorescein were elevated, confirming increased leakiness of the BBB (Fig. 7, A and B). TAK1 is upstream of the IKK complex. In the canonical NF-κB pathway, IKK2 phosphorylates and activates NF-κB. To analyze whether IKK2 mediates the effects of TAK1 on BBB integrity, we expressed a constitutively active mutant of IKK2 (IKK2CA) specifically in brain endothelial cells by crossing mice carrying the *R26-StopFLIkk2ca* (*Ikk2ca*^{Fl}) allele (Sasaki et al., 2006) with *Slco1c1-CreER*^{T2} animals. IKK2CA activated NF-κB, as shown by a lower steady-state level of the inhibitor IκBα in PBECs (Fig. 7 C) and elevated expression of the NF-κB target gene VCAM-1 in brain endothelial cells of *Tak1*^{beKO}*IKK2*^{beCA} mice

---

endothelial cells we perfused animals with 4% paraformaldehyde without post-fixation before staining. Representative images from one out of three mice per genotype are shown. Bar, 100 µm. Data are shown as means ± SEM. *, $P < 0.05$; **, $P < 0.01$; ***, $P < 0.001$, determined by repeated measures ANOVA with Fisher LSD post test (A), Student's *t* test (C), Mann-Whitney rank sum test (E), and two-way ANOVA with Bonferroni´s post test (B and H). Mice were investigated 19–24 d (E) or 28–32 d (A, C, and D) after start of tamoxifen treatment.

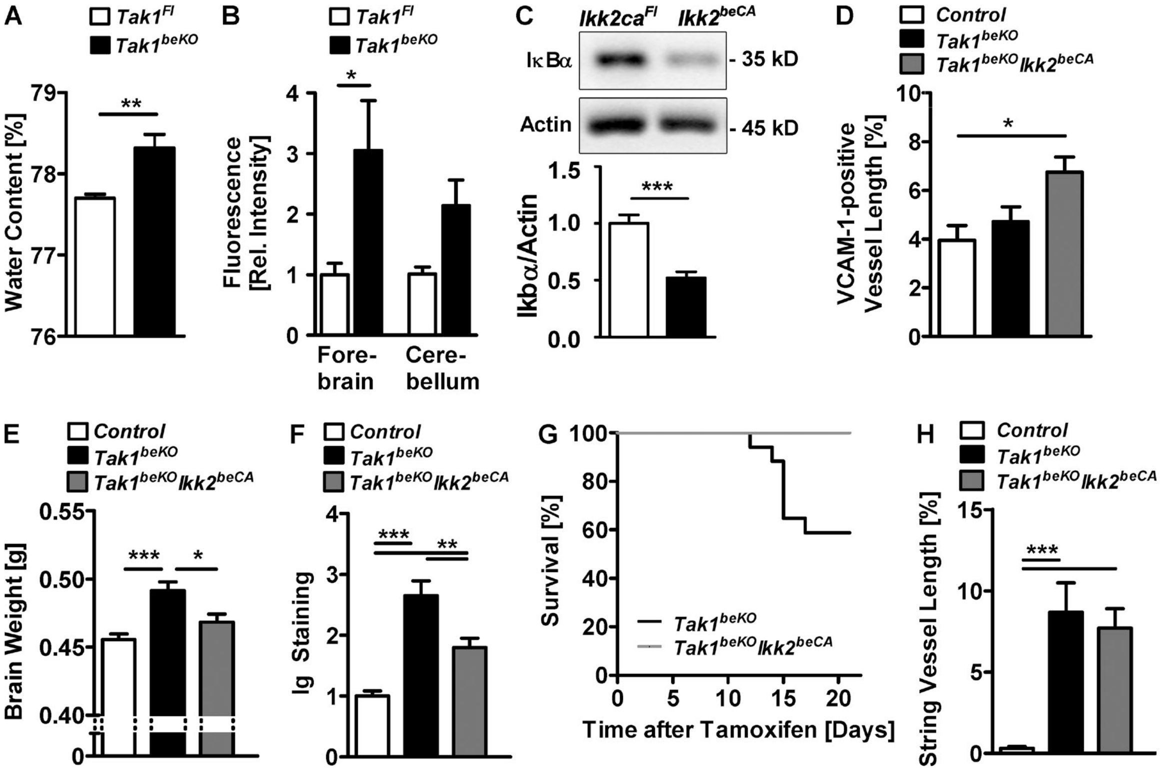

Figure 7. TAK1–NEMO signaling promotes BBB integrity via IKK2, whereas the effect on brain endothelial survival is independent of IKK2. (A) Brain water content in $Tak1^{beKO}$ and $Tak1^{Fl}$ mice is shown (n = 7–8). (B) BBB permeability in $Tak1^{beKO}$ and $Tak1^{Fl}$ mice was measured by fluorescein extravasation (n = 4). (C) Levels of the inhibitory IκBα in PBECs from $Ikk2^{beCA}$ mice were determined by Western blotting (n = 6). (D) Quantification of the vessel lengths expressing the endothelial NF-κB target gene VCAM-1 in the cortex of control, $Tak1^{beKO}$, and $Tak1^{beKO}Ikk2^{beCA}$ mice are shown (n = 5–9). In $Tak1^{beKO}Ikk2^{beCA}$ mice, *Tak1* is deleted and two copies of the *Ikk2ca* allele are overexpressed in brain endothelial cells. (E and F) Brain weight (E) and Ig staining (F) was quantified in control, $Tak1^{beKO}$, and $Tak1^{beKO}Ikk2^{beCA}$ mice (n = 9–14). (G) Survival curves of $Tak1^{beKO}$ and $Tak1^{beKO}Ikk2^{beCA}$ mice are shown (n = 21). $P < 0.01$ (log-rank test). (H) Quantification of string vessel lengths in the cortex 15 d after start of tamoxifen treatment (n = 10–14). Data are shown as means ± SEM. *, $P < 0.05$; **, $P < 0.01$; ***, $P < 0.001$, determined by two-way ANOVA with Bonferroni´s post test (B), one-way ANOVA with Tukey´s post test (D–F and H), and Student´s *t* test (A and C). Mice were investigated 7 d (B) or 15 d (A, D–F, and H) after start of tamoxifen treatment.

(Fig. 7 D). Overexpression of two copies of the *Ikk2ca* allele largely prevented the increase in brain weight and in brain Ig levels in $Tak1^{beKO}$ mice, confirming that TAK1 signals via IKK to maintain an intact BBB (Fig. 7, E and F). Additionally, overexpressing IKK2CA reduced the mortality of $Tak1^{beKO}$ mice (Fig. 7 G), supporting a causative relationship between BBB disruption and death of the mice. Although IKK2CA compensated for the TAK1 deficiency with respect to water content, Ig extravasation, and mortality, it did not prevent brain endothelial cell death induced by deleting *Tak1*, as the length of string vessels was not affected by IKK2CA overexpression (Fig. 7 H). This dissociation further supports the concept that different signaling pathways are effective downstream of TAK1 and NEMO in brain endothelial cells: an IKK2- and p65-dependent pathway stabilizing the BBB and an IKK2- and p65-independent pathway preventing endothelial cell death.

TAK1–NEMO–IKK2 signaling stabilizes the tight junction protein occludin

As the barrier properties of brain endothelial cells depend on their tight junctions, we investigated expression levels of tight junction proteins by immunostaining and Western blotting. Although protein levels of claudin-5 and ZO-1 were not changed (Fig. 8, A, B, F, and G), occludin expression was lower in the brains of $Nemo^{beKO}$ (Fig. 8, C–E) and $Tak1^{beKO}$ mice (Fig. 8 H) than in controls. IKK2CA overexpression restored occludin levels in TAK1-deficient mice (Fig. 8 H). Thus, TAK1 signals via IKK to sustain occludin expression and to preserve the integrity of the BBB. In support of a role of NF-κB signaling, occludin expression was also reduced in $p65^{beKO}$ mice (Fig. 8 I).

Dependence on NF-κB p65 suggests that occludin expression is regulated transcriptionally. Because *occludin* mRNA did not reflect the marked changes of its protein level in $Tak1^{beKO}$ mice (Fig. 8 J), we investigated whether an indirect mechanism regulates occludin protein. To evaluate the role of matrix metalloproteinases and the proteasome, which are able to degrade occludin (Cummins, 2012), we used small-molecule inhibitors in vitro. In PBECs of $Tak1^{beKO}$ mice or in wild-type PBECs treated with the TAK1 inhibitor 5Z-7-oxozeaenol (OZ), protein levels of occludin were reduced (Fig. 8, K, L and M). Down-regulation of occludin in OZ-treated cells

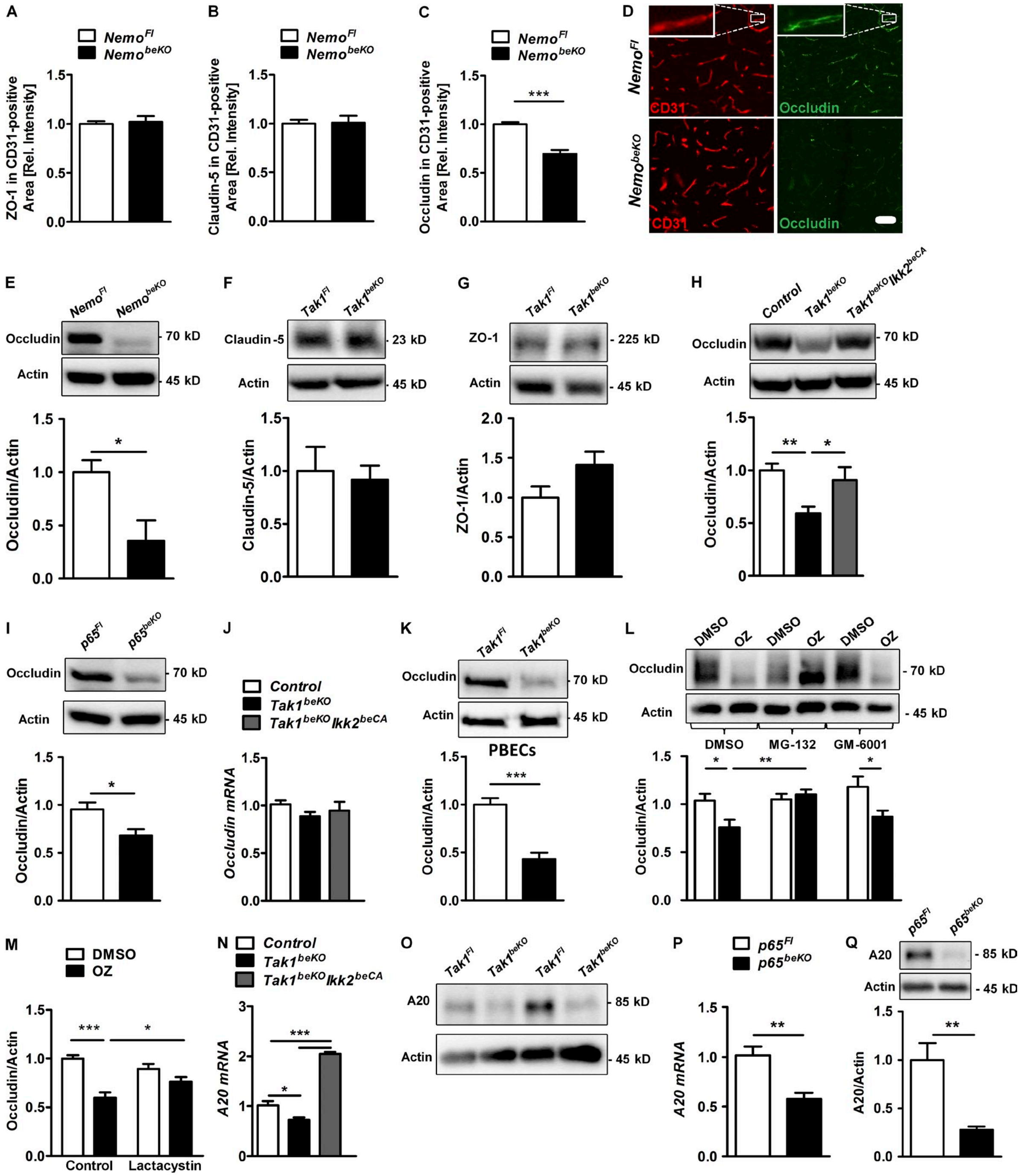

Figure 8. TAK1–NEMO inhibition leads to decrease of occludin and its deubiquitinase A20. (A–C) Quantifications of stainings of tight junction proteins ZO-1 (A), claudin 5 (B), and occludin (C). Sections were co-stained with anti-CD31 (*n* = 7–8). (D) Representative images of occludin staining are shown. (insets) High magnification of a capillary. (E) Western blotting of occludin in brain lysates of *Nemo*^{beKO} and control mice (*n* = 6). (F–I) Expression of claudin 5 (F), ZO-1 (G), and occludin (H and I) as determined by Western blotting in brain lysates of different mouse lines (*n* = 6–14). (J) *Occludin* mRNA levels were analyzed by real-time RT-PCR in brain lysates of *Tak1*^{beKO}, *Tak1*^{beKO}*Ikk2*^{beCA}, and control mice (*n* = 10–14). (K) Occludin protein levels in PBECs of *Tak1*^{Fl} and *Tak1*^{beKO} mice detected by Western blotting. (L–M) Effects of the proteasome inhibitors MG-132 (10 µM; L) or lactacystin (10 µM; M), as well as of the metalloproteinase inhibitor GM-6001 (10 µM; L) on occludin expression in PBECs was measured after treatment with the TAK1 inhibitor OZ (1 µM) for 24 h (*n* = 8–10) by Western blotting. (N–Q) Expression of A20, an occludin-targeting deubiquitinase, was measured in PBECs of *Tak1*^{beKO}*Ikk2*^{beCA}, *Tak1*^{beKO} (N and O) and *p65*^{beKO} (P and Q) mice as determined by real-time RT-PCR (N and P) and Western blotting (O and Q; *n* = 5–6). Data are shown as means ± SEM. *, $P < 0.05$; **, $P < 0.01$; ***, $P < 0.001$, determined by one-way ANOVA with Tukey's post test (H and N), Student´s *t* test (C, E, I, K, P, and Q), and two-way ANOVA with Bonferroni´s post test (L and M). Mice were investigated 15 d after start of tamoxifen treatment. Bar, 100 µm.

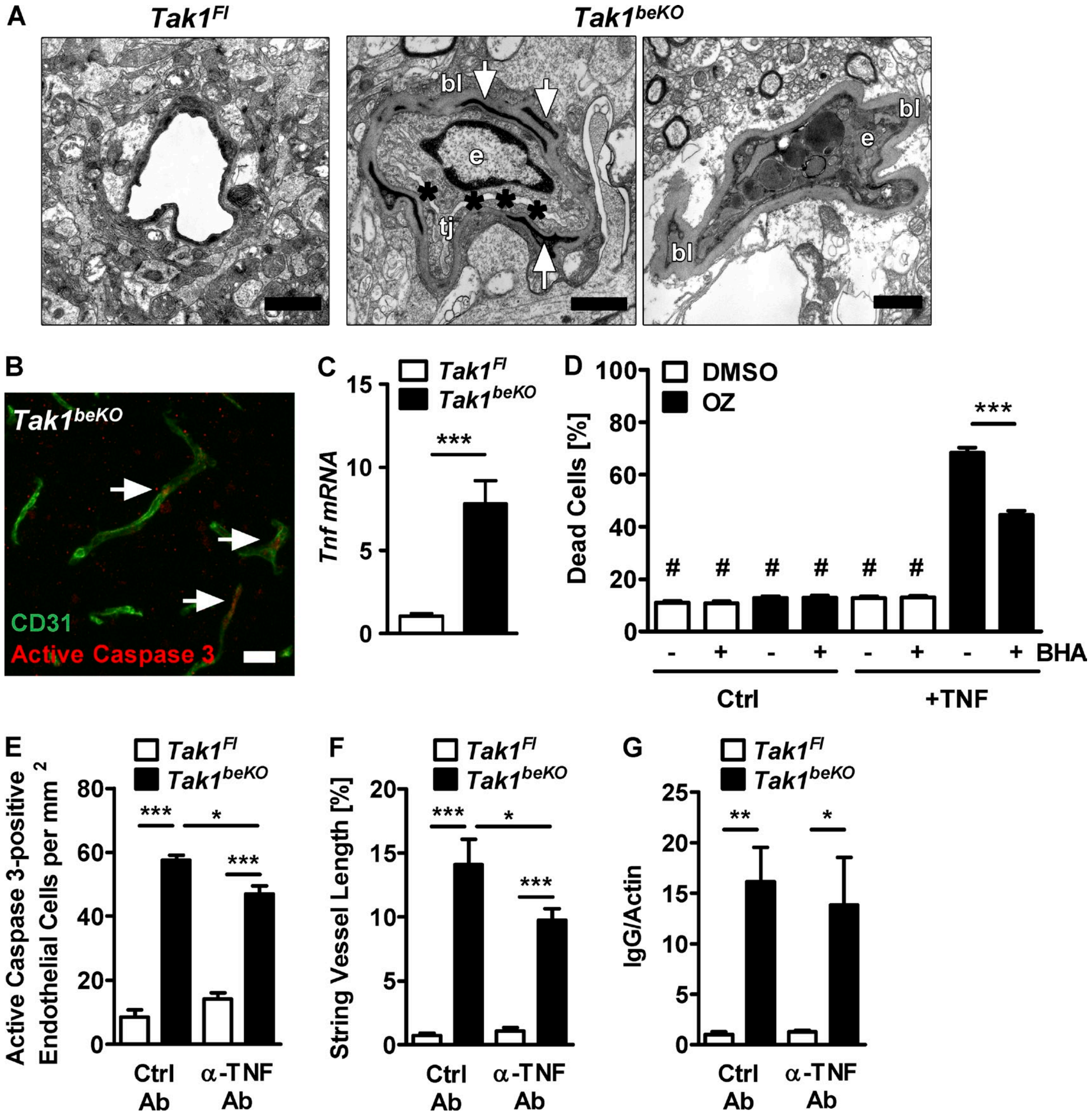

Figure 9. TNF mediates death of brain endothelial cells upon disruption of TAK1 signaling. (A) Electron microscopy showing signs of endothelial cell death and a thickened basal lamina (bl) in brains of *Tak1*^{beKO} mice. (left) Normal capillary of a *Tak1*^{Fl} mouse. (middle) Endothelial cell (e) of a *Tak1*^{beKO} mouse that is swollen; the lumen (asterisks) is obliterated; pericytes demonstrate signs of necrotic cytoplasm (arrows). tj, tight junction. (right) Endothelial cell (e) filled with electron-dark vacuoles; the basal lamina (bl) is thickened; lumen and tight junctions are no longer visible. (B) A representative immunostaining for active caspase 3 (arrows) and CD31 of *Tak1*^{beKO} cortex is shown. (C) *Tnf* mRNA was determined by real-time RT-PCR in brain lysates ($n = 6$). (D) Effects of TNF (50 ng/ml) and the TAK1 inhibitor OZ (1 µM) on cell death in brain endothelial bEnd.3 cells after 24 h. BHA, butylate hydroxyanisole (100 µM). #, $P < 0.001$ compared with groups treated with both TNF and OZ ($n = 11$). (E–G) The effect of neutralizing TNF antibodies (α-TNF Ab) on the number of active caspase 3–positive endothelial cells (E), string vessel formation (F), and IgG extravasation determined by Western blotting (G) in *Tak1*^{beKO} and *Tak1*^{Fl} mice is shown ($n = 3$–8). Data are shown as means ± SEM. *, $P < 0.05$; **, $P < 0.01$; ***, $P < 0.001$, determined by Student's *t* test (C) and two-way ANOVA with by Bonferroni's post test (D–G). Mice were investigated 10 d (A) or 14–15 d (B–G) after start of tamoxifen treatment. Bars: 1 µm (A); 50 µm (B).

was reversed by the proteasome inhibitors MG-132 or lactacystin but not by the broad metalloproteinase blocker GM-6001 (Fig. 8, L and M), demonstrating that the proteasome degrades occludin when TAK1 is inhibited. Ubiquitination labels occludin for proteasomal degradation (Cummins, 2012). An endothelial enzyme that deubiquitinates occludin and protects it from proteasomal degradation is A20 (*Tnfaip3*; Kolodziej et al., 2011). *A20* mRNA and protein levels were lower in TAK1- and in p65-deficient PBECs, whereas IKK2CA expression in PBECs of *Tak1*^{beKO}*IKK2*^{beCA} mice efficiently induced *A20* mRNA (Fig. 8, N–Q) in accordance with regulation of A20 expression by the TAK1–IKK–p65 pathway (Catrysse et al., 2014). Collectively, these data show that TAK1 and NEMO prevent occludin degradation by the proteasome, possibly by inducing A20 through NF-κB, and stabilize the BBB.

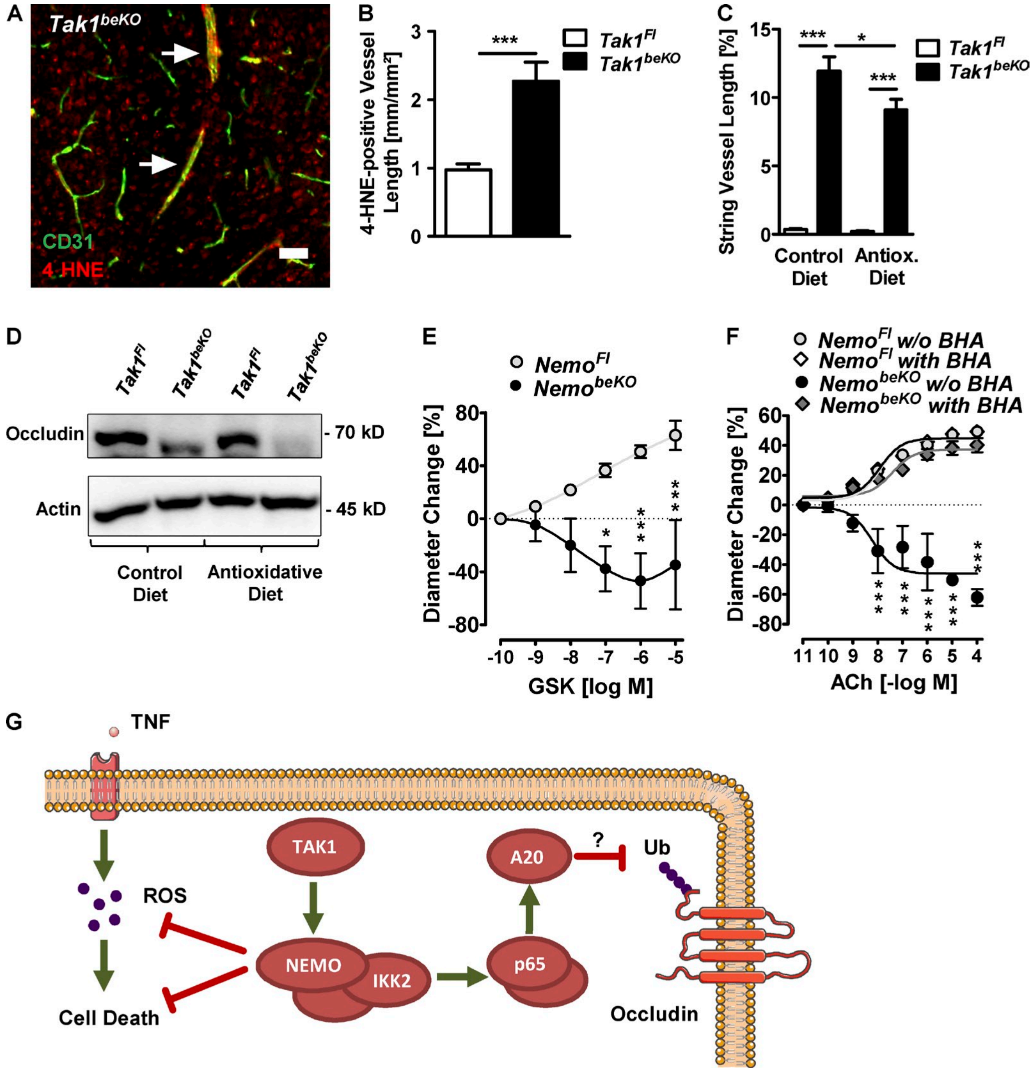

Figure 10. ROS mediate death of brain endothelial cells upon disruption of TAK1 signaling. (A and B) A representative immunostaining for 4-HNE, a marker for lipid peroxidation, in a *Tak1^{beKO}* mouse is shown (A). Quantification is shown in B (n = 5–7). (C and D) Effects of a diet containing the antioxidant BHA (0.7%) on string vessel formation (C) and occludin protein levels (D) in *Tak1^{beKO}* mice (n = 7–11). (E) Response of PCA segments of *Nemo^{Fl}* control and *Nemo^{beKO}* mice to the TRPV4 agonist GSK1016790A (GSK; n = 4–7). (F) The effect of BHA on the response of vessels isolated from *Nemo^{beKO}* mice were tested. Concentration-response curves for ACh are shown (n = 3–4). (G) Scheme summarizing the proposed mechanisms how TAK1 and NEMO prevent brain endothelial cell death and maintain the BBB. Ub, ubiquitination. Data are shown as means ± SEM. *, P < 0.05; ***, P < 0.001, determined by two-way ANOVA with Bonferroni's post test (C), repeated measures ANOVA with Bonferroni's post test (E and F), or Student´s *t* test (B). Mice were investigated 14–15 d (A–D), 14–18 d (E), or 19–22 d (F) after start of tamoxifen treatment. Bar, 50 µm.

Mechanisms of brain endothelial cell death upon disruption of TAK1–NEMO signaling

In electron microscopy, about half of the capillaries in *Tak1^{beKO}* mice were pathologically altered, showing a substantial thickening of the basement membrane (160–250 nm compared with a normal thickness of 40–60 nm; Fig. 9 A). Vessel lumina were obliterated due to swelling of endothelial organelles and cytoplasm, consistent with a necrotic form of endothelial cell death (Fig. 9 A). Together with the observed signs of apoptosis, i.e., staining for active caspase 3 in *Tak1^{beKO}* and *Nemo^{beKO}* mice (Figs. 2, A and B; and 9 B), this suggests that elements of necrosis and apoptosis occur in parallel.

TNF has been reported to induce cell death when TAK1–NEMO signaling is inhibited (Vanlangenakker et al., 2011; Xiao et al., 2011). Interestingly, in brains of *Tak1^{beKO}* mice, *Tnf* expression was elevated (Fig. 9 C). In brain endothelial bEnd.3 cells, TNF strongly triggered cell death if TAK1 signaling was inhibited by OZ (Fig. 9 D). Therefore, we treated *Tak1^{beKO}* mice with TNF-neutralizing antibodies. Anti-TNF partially protected against brain endothelial cell death as revealed by less endothelial cells positive for active caspase 3 and shorter lengths of string vessels (Fig. 9, E and F). However, TNF neutralization in the same animals did not significantly reduce BBB disruption as shown by a similar Ig brain content (Fig. 9 G).

Previous studies have demonstrated that TAK1–NEMO signaling protects against TNF-induced death of other cell types by down-regulating reactive oxygen species (ROS; Xiao et al., 2011; O'Donnell et al., 2012; Dondelinger et al., 2013). In *Tak1*^{beKO} mice, we observed an increase in brain vessels positive for the lipid peroxidation product 4-hydroxy-nonenal (4-HNE), indicating ROS production (Fig. 10, A and B). The antioxidative agent butylated hyroxyanisole (BHA) inhibited TNF-induced cell death when TAK1 was blocked in vitro (Fig. 9 D) and reduced the occurrence of string vessels in *Tak1*^{beKO} mice in vivo (Fig. 10 C); this gives evidence for the involvement of ROS in endothelial cell death. In contrast, BHA treatment did not prevent occludin down-regulation in *Tak1*^{beKO} mice (Fig. 10 D). Thus, when TAK1–NEMO signaling is inhibited, endothelial cell death is partially dependent on TNF and ROS but not on IKK2 and p65.

Because ROS are a well-known cause of endothelial dysfunction in arteries (Girouard and Iadecola, 2006), we asked whether ROS production could also underlie the impaired cerebrovascular reactivity in *Nemo*^{beKO} mice. The ROS-sensitive endothelial cation channel TRPV4 largely mediates endothelial dilation induced by acetylcholine (Sonkusare et al., 2012; Zhang et al., 2013). Dilations of PCAs in response to GSK1016790A (GSK), a selective TRPV4 agonist, were impaired if the vessels were isolated from *Nemo*^{beKO} mice, in accordance with the notion that ROS mediate endothelial dysfunction upon *Nemo* deletion (Fig. 10 E). Indeed, scavenging ROS by pretreating PCA segments of *Nemo*^{beKO} mice with BHA fully rescued the impaired dilatory response to acetylcholine (Fig. 10 F).

Together, NEMO and TAK1 use distinct mechanisms that differentially depend on IKK2 and p65 NF-κB, as well as TNF and ROS to support the survival of brain endothelial cells, regulate cerebrovascular reactivity, and protect the BBB (Fig. 10 G).

DISCUSSION

Patients with CNS involvement of IP usually present with the clinical picture of an acute encephalopathy, signs of which include a reduced motivational drive and epileptic seizures (Hennel et al., 2003; Abe et al., 2011; Meuwissen and Mancini, 2012). Diffusion-weighted MR imaging in IP patients indicated cytotoxic brain edema that occurs in cerebral ischemia (Hennel et al., 2003; Abe et al., 2011). However, large cerebral arteries are not occluded in most IP patients (Hennel et al., 2003; Maingay-de Groof et al., 2008). This seeming contradiction is resolved by the finding of small vessel pathology. IP is caused by heterozygous mutations in the X-chromosomal *Nemo* gene and *Nemo*$^{-/+}$ mice mimic the skin manifestations of IP (Makris et al., 2000; Schmidt-Supprian et al., 2000). In the brain of *Nemo*$^{-/+}$ mice, we have detected so-called string vessels as a conspicuous sign of small vessel pathology that corresponds well to the clinical imaging data. String vessels are empty basement membrane strands without inner endothelial cells and without perfusion. A vascular cause of the neurological symptoms in IP is supported by the finding that cell type–specific deletion of *Nemo* in neurons and glial cells did not lead to any obvious deficits (Fig. 1 B; van Loo et al., 2006), whereas deletion in brain endothelial cells (*Nemo*^{beKO}) induced a phenotype that resembles the clinical disease in several aspects. In accordance with a reduced motivational drive, *Nemo*^{beKO} mice showed signs of anorexia and less sociability but more anxiety-like behavior. Very much like IP patients, *Nemo*^{beKO} mice had focal and generalized tonic-clonic seizures that seem to cause the increased mortality in the mouse model. Further support for the notion that *Nemo*^{beKO} mice are a model of the CNS involvement in IP patients comes from the detection of string vessels in the brain of an IP patient, although we were only able to investigate a single patient at this stage.

Rarefaction of capillaries and string vessels in *Nemo*^{beKO} mice are explained by the death of endothelial cells. The signs of endothelial necrosis and apoptosis in the absence of TAK1 or NEMO were neither rescued by overexpression of IKK2CA nor mimicked by deletion of *p65* NF-κB. In contrast to the general notion that NEMO exerts its effects via NF-κB, these findings indicate that TAK1 and NEMO can prevent cell death independent of NF-κB, at least of the p65 subunit and its main activator in the canonical pathway, IKK2. Previous work has already shown in vitro that TAK1 and NEMO can prevent TNF-induced cell death without the need for NF-κB–mediated gene transcription (O'Donnell et al., 2012; Dondelinger et al., 2013). Our study now provides the first in vivo evidence for this novel function of TAK1 and NEMO in brain endothelial cells. Interestingly, the effects of TAK1 or NEMO deficiency on survival differ between cell types. Neural cells, for instance, are resistant to TAK1 or NEMO deficiency (van Loo et al., 2006; Goldmann et al., 2013). In peripheral endothelial cells TAK1 deficiency leads to vessel regression and reduced cell migration during embryogenesis (Morioka et al., 2012). Based on the current data, we cannot exclude that NEMO has a similar role in peripheral endothelial cells. However, the inducible deletion of *Nemo* in peripheral endothelial cells of adult mice prevented atherosclerotic changes (Gareus et al., 2008). Accordingly, IP patients do not suffer from peripheral vascular problems. In contrast, in the brain, deletion of *Tak1* or *Nemo* compromised the survival of endothelial cells, underlining the distinct features of these cells in the CNS.

In *Nemo*^{beKO} and *Tak1*^{beKO} mice, death of endothelial cells led to a rarefaction of capillaries with a shorter total vessel length. Capillary pathology translates into hypoperfusion under basal conditions and, intriguingly, it may also explain why neurovascular coupling was impaired. According to a recent reanalysis of the flow–diffusion equation, an increased heterogeneity of capillary transit time caused by capillary pathology is associated with a deficit in neurovascular coupling (Ostergaard et al., 2013). Finally, *Nemo* deletion also affected large cerebral arteries. Endothelium-dependent stimuli were less effective in dilating the PCA of *Nemo*^{beKO} mice than of control animals. However, the antioxidant BHA rapidly normalized dilation in *Nemo*^{beKO} mice, suggesting that ROS impair endothelial function in the absence of endothelial NEMO. Thus, endothelial dysfunction of cerebral arteries and the loss of cerebral capillaries compromise cerebral blood flow in *Nemo*^{beKO} mice.

In addition to endothelial cell death, *Nemo*^{beKO} mice showed signs of a disturbed BBB and vasogenic brain edema, very much like IP patients with acute neurological manifestations (Avrahami et al., 1985; Chatkupt et al., 1993). Conceivably, gaps in the endothelial lining of cerebral blood vessels after endothelial cell loss might increase BBB permeability. However, our data demonstrate that disruption of the BBB and endothelial cell death are at least partially independent (Fig. 10 G), suggesting that capillaries with gaps in the endothelial lining are shut down before a major leak occurs. To safeguard the BBB, TAK1 and NEMO trigger an IKK2- and p65 NF-κB–mediated pathway that ultimately up-regulates the tight junction protein occludin by limiting its proteasomal degradation. Occludin is possibly stabilized due to induction of A20, a well-established target gene of NF-κB that is able to deubiquitinate occludin (Kolodziej et al., 2011).

Previous studies reported that NF-κB activation in brain endothelial cells is associated with increased permeability of the BBB, suggesting that endothelial NF-κB may promote disruption of the barrier (Alvarez et al., 2013). However, when we deleted components of NF-κB signaling exclusively in brain endothelial cells, we found that NF-κB actually protects the BBB, at least under the basal conditions that we have investigated. At present, we cannot exclude that under inflammatory conditions the situation might be different and high levels of endothelial NF-κB activity could damage the BBB, in the sense of a bell-shaped relationship between NF-κB activity and BBB integrity. However, this assumption is not necessarily required, because NF-κB–independent mechanisms that are instead mediated by ARNO, ARF6, β-catenin, and FoxO1 increase endothelial permeability in response to inflammatory factors (Zhu et al., 2012; Beard et al., 2014). In addition, activation of NF-κB in neighboring astrocytes and pericytes leads to the release of inflammatory mediators that subsequently break down the BBB (Zhang et al., 2007; Bell et al., 2012). An attractive hypothesis is that the NF-κB–mediated endothelial pathway identified by us serves to reverse the increased permeability of the BBB in the presence of inflammation.

Occludin is an integral component of tight junctions but is apparently not required for their normal morphology (Saitou et al., 2000). It is the claudin family of molecules that is mainly responsible for the barrier. Nevertheless, brain calcifications in occludin knockout mice hint to a BBB disturbance (Keller et al., 2013) and the acute interference with occludin function leads to an overt disruption of barriers (Everett et al., 2006), supporting the notion that occludin plays a modifying role in the BBB. As tight junctions and a high occludin expression are characteristic of brain endothelial cells (Hirase et al., 1997), it is expected that the TAK1–NEMO–NF-κB signaling pathway-stabilizing occludin expression in brain endothelial cells may be less important for the tightness of peripheral vessels. However, our study did not address the contribution of NEMO to the permeability of the vasculature in other organs and previous studies have reported divergent findings for the role of NF-κB in the permeability of peripheral endothelial cells (Kisseleva et al., 2006; Ye et al., 2008).

Disruption of the BBB occurs in several pathological conditions, including traumatic brain injury, cerebral ischemia, and infections, all of which are associated with an increased risk of epilepsy. The concept that BBB breakdown induces epileptic seizures (Seiffert et al., 2004; Obermeier et al., 2013) is supported by our observation that brain endothelial-specific deletion of *Nemo* leads to epilepsy in *Nemo*^{beKO} mice. After leaking through the BBB, albumin triggers epileptic activity by transforming astrocytes (Ivens et al., 2007). Thus, the high amount of albumin in brain tissue of *Nemo*^{beKO} mice and the activation of astrocytes are likely causes of epileptic seizures and may serve as an explanation for the relationship between *Nemo* mutations and the development of epilepsy in IP patients.

A dense vascular network and the BBB are essential prerequisites for brain function. Proinflammatory mediators open the BBB and disrupt microvascular perfusion, and therefore put brain homeostasis at risk. Our data now show that brain endothelial cells actually rely on an inflammatory pathway, TAK1–NEMO signaling, to maintain normal brain function. Thus, brain endothelial-specific deletion of *Nemo* in mice mimics the neurological symptoms of IP. On the basis of these data, neutralizing TNF antibodies, antioxidative substances such as BHA, or gene therapy with AAV vectors that selectively target brain endothelial cells (Chen et al., 2009) may provide rational treatment options for the neurological symptoms of IP.

MATERIALS AND METHODS

Mice. All mouse lines were established on a C57BL/6 background. We used littermate mice that were sex- and age-matched between experimental groups. In most experiments, mice were between 6 and 18 wk of age. All animal experiments were approved by the local animal ethics committee (Regierungspräsidium Karlsruhe; Ministerium für Landwirtschaft, Umwelt und ländliche Räume, Kiel, Germany). Heterozygous *Nemo* knockout mice (*Nemo*$^{-/+}$) were generated by crossing *Nemo*^{Fl} mice (Schmidt-Supprian et al., 2000) with *CMV-Cre* mice (Schwenk et al., 1995). For neuronal and glial knockout of Nemo (*Nemo*^{ngKO}) we crossed *Nemo*^{Fl} mice with the *Nestin-Cre* line (Tronche et al., 1999). Brain endothelial-specific knockout (beKO) animals were generated by crossing the BAC-transgenic *Slco1c1-CreER*^{T2} strain (Ridder et al., 2011), which expresses the tamoxifen-inducible CreER^{T2} recombinase under control of the mouse *Slco1c1* regulatory sequences in brain endothelial cells and epithelial cells of the choroid plexus, with mice carrying different loxP-flanked alleles (*Nemo*^{Fl}; Schmidt-Supprian et al., 2000), p65GFP^{Fl} (De Lorenzi et al., 2009), *Tak1*^{Fl} (Sato et al., 2005), *Traf6*^{Fl} (Polykratis et al., 2012), or the Cre reporter line B6.Cg-Gt(ROSA)26Sor$^{tm14(CAG-tdTomato)Hze}$/J (Ai14; Madisen et al., 2010). Mice with a brain endothelial deletion of *Tak1* and overexpression of constitutively active IKK2 were created by crossing *Tak1*^{beKO} mice with *R26-StopFLIkk2ca* (*Ikk2ca*^{FL}) mice (Sasaki et al., 2006). Mice were homo- or hemizygous for all loxP-flanked alleles with the exception of a group depicted in Fig. 1 G. All transgenic animals used in this study were injected with 1 mg tamoxifen dissolved in 90% miglyol 812/10% ethanol i.p. every 12 h for 5 consecutive days. Littermates lacking the Cre transgene were used as controls in all experiments. TNF function was blocked by injecting *Tak1*^{beKO} and *Tak1*^{Fl} mice i.p. weekly with TNF-neutralizing (0.2 mg, clone CNTO5048) or control antibodies (0.2 mg, clone CNTO1322) starting 1 d before tamoxifen treatment until the end of the experiment (15 d after the first tamoxifen injection). For antioxidative diet, animals were fed with BHA-enriched (0.7%; Ssniff) or control food starting 2 wk before tamoxifen treatment. We did not exclude mice from analysis unless they died before the endpoint was measured. Mice were randomly allocated to diet or treatment groups. Investigators were blinded for treatment or genotype of mice or both in all experiments and analyses.

Histological quantifications. We perfused mice with PBS containing heparin (10 IU/ml) to minimize vascular Ig staining. To quantify endogenous Ig extravasation, cryosections were stained with Cy3-labeled donkey anti-mouse IgM antibodies upon methanol fixation. The intensity of two to four pictures per mouse was determined with ImageJ software (National Institutes of Health) and values were expressed relative to control animals. The same procedure was used to determine GFAP in cortical tissue stained with anti-GFAP antibodies. String vessels were defined as empty basement membrane tubes and quantified by measuring the length of collagen IV–positive and CD31-negative vessels with ImageJ software. Vessel length was measured in anti-CD31–stained sections. Two to four images were taken in the cortex if not stated otherwise, and analyzed for all parameters. To detect string vessels in human paraffin-embedded brain samples, we performed antigen-retrieval procedures before staining and used anti–collagen IV and anti-CD34, an endothelial cell marker. The Ethics Committee of the University of Lübeck was informed about the study.

For quantifying 4-HNE- or active caspase 3–positive vessels, cryosections were stained with anti–4-HNE or anti-active caspase 3 and CD31. Measurements were performed as described for string vessels.

Stainings for CD31, collagen IV, pan-laminin, laminin α5, and SMA were quantified in a partially automated manner using a custom macro implemented into the image analysis software Fiji. In brief, images were thresholded using an auto-threshold method, despeckled, and smoothened to remove staining artifacts. After conversion into a binary image, staining length was quantified with the Skeleton 2D/3D plugin yielding the number and length of stained structures in each image. To ensure reliable quantification, the macro was initially compared with a manually quantified dataset showing a significant correlation ($r^2 = 0.9157$; unpublished data).

For the quantification of tight junction proteins (ZO-1, claudin-5, and occludin) on histological stainings, double-staining against the protein of interest and CD31 was performed. A selection of the vessel area was created by thresholding the CD31-image with an auto-threshold method. The thresholded image was used to create a mask, which then was applied onto the image showing the staining for the tight junction protein. The mean intensity was determined for this mask.

The staining for GFP in $p65^{Fl}$ and $p65^{beKO}$ mice was performed on 100-µm vibratome slices after short perfusion of the animals with 4% paraformaldehyde without post-fixation. Sections from one experiment were always stained in parallel; images were generated at the same magnification, fluorescence excitation intensity, and gain.

Biotin angiography. Mice were i.v. injected with sulfo-NHS-LC-biotin (EZ-Link; 5 mg/100 µl per mouse; Thermo Fisher Scientific). 60 min later, mice were perfused with PBS and killed. The biotin was labeled on cryosections with Alexa Fluor 488–coupled Streptavidin (1:1,000; Invitrogen).

Determination of brain water content and BBB permeability. After dissection, brains were weighed immediately and dried for 4 d at 85°C. The percentage of water content was calculated as (wet weight − dry weight) × 100/wet weight.

To investigate the permeability to sodium fluorescein, mice were injected i.v. with sodium fluorescein (6 mg/ml dissolved in PBS, 200 µl per 25 g body weight; Schoch et al., 2002). 30 min later, anesthetized mice were transcardially perfused with 10 ml of ice-cold Ringer´s solution. Forebrain and cerebellum were homogenized in 0.5 M sodium perborate dissolved in dH_2O and centrifuged (800 *g*) for 15 min at 4°C. Ethanol (1.2 ml) was added to the supernatant and the samples were again centrifuged (16,100 *g*) for 20 s before measurement of fluorescence in the supernatant.

Dextrans of various sizes labeled with FITC (BD) were suspended in PBS (4 and 70 kD, 12 mg/ml; 150 and 2,000 kD, 24 mg/ml; Carman et al., 2011) and injected (100 µl per mouse) i.v. 2 h later, anesthetized mice were perfused and brains were homogenized in 50 mM Tris-HCl, pH 8.0 (500 µl per hemisphere). After centrifugation (16.1 *g* for 30 min), equal volumes of methanol were added to supernatants. After another centrifugation (16.1 *g* for 15 min), fluorescence in supernatants was detected at 528 nm with an excitation wavelength of 485 nm using a microplate reader (Fluostar Optima).

EEG monitoring. For the recording of EEG, cortical screw electrodes were stereotactically implanted under anesthesia with ketamine (70 mg/kg i.p.) and xylazine (14 mg/kg i.p.) above the dorsal hippocampus or the fronto-parietal cortex (coordinates from bregma: AP −1.7; L +/−1.6 or AP +3.0; L +/−1.5, respectively) in 6 $Nemo^{beKO}$ and 2 $Nemo^{Fl}$ mice per electrode location. Furthermore, a control group of 10 wild-type C57BL/6 mice received fronto-parietal cortex screws. To prevent postoperative infection, mice were treated with marbofloxacin (4 mg/kg, s.c., once daily) for 7 d starting 2 d before electrode implantation.

2 wk after surgery, mice were treated with tamoxifen. For continuous (24 h/d) EEG-monitoring, mice were connected to the system consisting of one-channel amplifiers (Animal BioAmp ML136; ADInstruments) and analogue-digital converters (PowerLab 8/30 ML870; ADInstruments) via a flexible cable. The data were recorded and analyzed with the LabChart 6 software (ADInstruments; sampling rate 200 Hz; time constant 0.1 s; low pass filter 60 Hz). The EEG recording was directly linked to simultaneous digital video-recording using one high-resolution infrared camera for up to eight mice (NYCTO Vision; CaS Business Services). For monitoring during the dark phase, infrared LEDs were mounted above the cages. The monitoring period started at day 8 after beginning of the tamoxifen treatment and lasted 7–18 d depending on the detection of epileptiform activity. In addition, mice were observed by two experimenters for 1 h per day for 5 d to detect myoclonic twitches. Wild-type mice were recorded once for one week.

Antibodies and chemicals. For Western blotting and immunofluorescent staining, the following antibodies and dilutions were used: anti–4-hydroxynonenal (4-HNE) 1:1,000 (EMD Millipore); anti-actin 1:1,000 (Santa Cruz Biotechnology, Inc.); anti–active-caspase-3 1:400 (Cell Signaling Technology); anti-CD31 1:500 (BD or Santa Cruz Biotechnology, Inc.); anti-CD34 1:50 (Leica); anti-aquaporin 4 1:100 (EMD Millipore); anti-CD13 1:400 (AbD Serotec); anti-GFP 1:2,000 (Abcam); anti-GFAP 1:500 (Dako); anti-SMA 1:200 (Acris); anti–pan-laminin 1:1,000 (Wu et al., 2009); anti-laminin α5 1:200 (Sorokin et al., 1997); anti–claudin-5 1:200 (Invitrogen); anti-collagen IV 1:1,000 (Abcam); anti-IκBα 1:500 (Santa Cruz Biotechnology, Inc.); anti-NEMO 1:500 (Santa Cruz Biotechnology, Inc.); anti–NF-κB p65 1:500 (Santa Cruz Biotechnology, Inc.); anti-occludin 1:500 (Abcam or Proteintech; 1:1,000); anti-TAK1 1:500 (Cell Signaling Technology); anti-TRAF6 1:500 (Santa Cruz Biotechnology, Inc.); anti-ZO1 1:250 (Invitrogen); anti–VCAM-1 1:1,000 (BD); anti–mouse-IgM-Cy3 1:400 (Jackson ImmunoResearch Laboratories); anti–mouse-IgG-HRP 1:5,000 (Santa Cruz Biotechnology, Inc.). Butylated hydroxyanisole (BHA), MG-132, sodium perborate, sodium fluorescein, and tamoxifen were obtained from Sigma-Aldrich. 5Z-7 OZ was purchased from Tebu-Bio. GM-6001 was obtained from Merck. Lactacystin was purchased from Santa Cruz Biotechnology, Inc. The diet containing 0.7% BHA and the respective control diet were manufactured by Ssniff. Anti-murine TNF (clone CNTO5048) and isotype-matched control antibodies (clone CNTO1322) were provided by D. Shealy (Janssen R&D, Raritan, NJ). Mouse TNF was obtained from PeproTech.

Cell culture. PBECs of mice were cultured as described previously (Ridder et al., 2011). bEnd.3 cells (ATCC) were grown in DMEM containing FCS (10%), glucose (4.5 g/liter), penicillin (100 IU/ml), streptomycin (100 µg/ml), and L-glutamine (2 mM). Cell death was measured using the Cytotoxicity Detection kit (LDH; Roche) according to the manufacturer´s instructions.

Western blotting. If not indicated otherwise, the cerebellum was homogenized in cell lysis buffer (Cell Signaling Technology) supplemented with

0.5 M PMSF directly before use. PBECs were cultured on 6-well plates and lysed in hot 2× Laemmli buffer, incubated at 95°C for 5 min, and then loaded on SDS-PAGE gels. Proteins were transferred to nitrocellulose membranes, which were then incubated with the indicated primary antibodies overnight at 4°C and, subsequently, with HRP-conjugated secondary antibodies for 1–2 h at room temperature. For detection, we applied enhanced chemiluminescence (SuperSignal West Femto Substrate; Thermo Fisher Scientific) and a digital detection system (GelDoc 2000; Bio-Rad Laboratories).

In vivo MRI acquisition. Mice were anesthetized with an induction dose of 4–5% sevoflurane and secured in an MRI-compatible bed. All MRI studies were performed under ∼2.5–3% sevoflurane in medical air and animals were allowed to breathe spontaneously. Respiration rate and body temperature was continuously monitored using an MRI-compatible system (Small Animal Instruments Inc.), and the temperature was maintained at 37 ± 0.2°C throughout the study using a feedback-regulated warming system (Small Animal Instruments Inc.).

All MR images were acquired on a 7 T Bruker Pharmascan system (Bruker Biospin) using a 28-mm inner-diameter, quadrature volume resonator (RAPID MR International) and using previously established methods (Grand'Maison et al., 2013; Hébert et al., 2013). In brief, after the acquisition of scout images, ROI-based shimming (MAPSHIM; Bruker Biospin) was performed to increase the magnetic field homogeneity within the brain. Anatomical images were acquired using a 3D balanced Steady-State Free Precession (b-SSFP) sequence with matrix size = 128 × 128 × 64, field-of-view = 1.8 × 1.8 × 0.9 cm, spatial resolution = 140 × 140 ×140 μm, number of phase-cycles = 4, and number of averages = 4. The phase-cycled images were combined using the sum-of-squares reconstruction method to minimize banding artifacts (Bangerter et al., 2004). Perfusion images were acquired with a customized, 3D pseudocontinuous arterial spin labeling (ASL) sequence with matrix size = 64 × 64 × 32, field-of-view = 1.8 × 1.8 × 0.9 cm, spatial resolution = 280 × 280 × 280 μm, and 48 averages. Perfusion labeling was achieved by positioning a 2-mm-thick inversion slab in the neck region (∼7 mm inferior to the level of the brainstem) and inverting inflowing blood within this slab every 14 ms using spatially selective sinc radiofrequency pulses. The entire scanning session lasted ∼2.5 h per animal.

MRI processing. An unbiased, symmetric, customized template was generated from anatomical scans from the 25 mice using an iterative process (Lau et al., 2008; Fonov et al., 2011). Before template generation, each reconstructed image volume underwent image nonuniformity correction using the N3 algorithm (Sled et al., 1998), brain masking, and linear spatial normalization using a 12-parameter affine transformation (Collins et al., 1994) to map individual images from native coordinate space to reference space. In brief, the template-generation process involved an iterative (coarse-to-fine resolution) estimation of the nonlinear transformation to match each MRI scan to the evolving average of the population. The final anatomical template (population average) was generated with an isotropic voxel resolution of 0.06 mm. This customized template was parcellated into an atlas consisting of the whole cortex, the hippocampus, and the lateral ventricles using the Montreal Neurological Institute (MNI) McConnell Brain Imaging Centre DISPLAY software package. The mask of the cortex was projected onto a standardized cortical surface template.

The control perfusion images were linearly registered to the anatomical images for each mouse to compensate for potential, slight movement during the scanning session. Parametric perfusion maps based on the fractional ASL signal, defined as the ratio between the difference [control − labeled] and control images (Hébert et al., 2013), were calculated on a voxel-by-voxel basis. The perfusion maps were spatially normalized to reference space using the transformations derived from the anatomical image registration. The individual, spatially normalized perfusion maps were averaged to produce group-mean parametric maps. ROI-based perfusion measures were derived using the MRI atlas in reference space.

NF-κB luciferase assay. After 5 d in vitro, PBECs were infected with an adenovirus carrying a NF-κB luciferase reporter gene (Ad-NFKb-Luc; Vector Biolabs) in medium with reduced (2%) serum concentration for 30 h, subsequently incubated in serum-free medium for 18 h, and stimulated with murine TNF (10 ng/ml) for 4 h. Cells were then washed once with PBS and harvested in glycylglycine buffer (25 mM glycylglycine, 15 mM $MgSO_4$, and 4 mM EDTA) containing 1% Triton X-100 and 1 mM DTT. Luciferin solution (50 μl; 1 μM d-luciferin [Sigma-Aldrich] in glycylglycine buffer containing 10 μM DTT) and 92 μl assay buffer (16.3 mM KH_2PO_4, 1.09 mM DTT, 2.17 mM ATP dissolved in glycylglycine buffer) were added to 25 μl of cell lysate. Firefly luciferase activity was determined with a microplate reader (Fluostar Optima; BMG Labtech) and normalized to protein content measured by Advanced Protein Assay Reagent (Cytoskeleton).

Real-time RT-PCR. RNA was isolated from cerebellum or PBECs by using the ABI Prism 6100 Nucleic Acid PrepStation (Applied Bioscience) according to the manufacturer's instructions. RNA (400 ng) was transcribed with Moloney Murine Leukemia Virus Reverse transcription and random hexamer primers (Promega). The following primers were used for quantitative RT-PCR: *Ocln* forward, 5′-TACTGGTCTCTACGTGGATCAAT-3′, *Ocln* reverse, 5′-TTCTTCGGGTTTTCACAGCAA-3′, PCR product 137 bp; *Ppia* forward, 5′-AGGTCCTGGCATCTTGTCCAT-3′, *Ppia* reverse, 5′-GAACCGTTTGTGTTTGGTCCA-3′, PCR product 51 bp; *Tnf* forward, 5′-TGTAGCCCACGTCGTAGCAAA-3′, *Tnf* reverse, 5′-GCTGGCACCACTAGTTGGTTGT-3′, PCR product 120 bp; *Tnfaip3* forward, 5′-ACAGTGGACCTGAACTTCGC-3′, *Tnfaip3* reverse, 5′-TGCACAGGGATCTCCATCAC-3′, PCR product 151 bp. Quantitative RT-PCR was performed according to the following protocol: 2 min at 50°C, 2 min at 95°C, 15 s at 95°C, and 1 min at 60°C (40 cycles). Amplification was quantified using Platinum SYBR Green qPCR SuperMix (Invitrogen). Quantified results were normalized to *Ppia* using the ΔΔCt method.

Cerebrovascular reactivity. Cerebrovascular dilatory and contractile function was tested in vitro in isolated, cannulated, and pressurized (60 mm Hg) segments of the PCA isolated from $Nemo^{beKO}$ or $Nemo^{Fl}$ mice. We used online video microscopy to monitor diameter changes (Tong et al., 2005, 2012). Concentration-dependent dilations to ACh (Sigma-Aldrich) were tested on vessels preconstricted with phenylephrine (200 nM; Sigma-Aldrich). The contractile response to endothelin-1 (American Peptide) was tested on vessels at resting tone as was the tonic production of nitric oxide (NO) measured by superfusion with the NO synthase inhibitor *N*ω-nitro-L-arginine (L-NNA; 10 μM, 40 min; Sigma-Aldrich). Because TRPV4 channels are involved in the ACh-induced dilation of cerebral arteries (Zhang et al., 2013), their function was tested in preconstricted vessels with the TRPV4 selective agonist GSK1016790A. The dilatory capacity of the vessels was verified with the NO donor sodium nitroprusside. Reversibility of the vascular deficits in response to ACh was tested before and after preincubation (30–60 min) of the arterial segments with the antioxidant butylated hydroxyanisole (BHA, 100 μM).

Electron microscopy. For electron microscopy, $Tak1^{Fl}$ and $Tak1^{beKO}$ mice were transcardially perfused with 2.5% glutaraldehyde (Paesel and Lorei) in 0.1 M cacodylate buffer (pH 7.4). Brains were isolated and postfixed in 2.5% glutaraldehyde for 2–4 h, and then stored in cacodylate buffer. Brain cortices were cut into small pieces and washed once with 0.1 M cacodylate buffer. The specimens were postfixed in 1% OsO_4 in cacodylate buffer for 1 h and dehydrated in ascending series of ethanol and propylene oxide. For contrast enhancement, they were bloc stained in uranyl acetate in 70% ethanol for 4 h and flat-embedded in Araldite (Serva). Using an ultramicrotome (Ultracut R; Leica), semithin (1 μm) and ultrathin (50 nm) sections were cut. Ultrathin sections were stained with lead citrate, mounted on copper grids, and finally analyzed with an EM 10 electron microscope (Carl Zeiss).

Laser doppler flowmetry (LDF). LDF measurements of cerebral blood flow were performed as described previously (Tong et al., 2009). Mice were anesthetized with ketamine (85 mg/kg, i.m.) and xylazine (3 mg/kg, i.m.) and placed in a stereotaxic frame on a heating blanket to maintain a stable body temperature (37°C). The skull over the barrel cortex was thinned to translucency for the placing of the LDF probe. Contralateral cerebral blood flow was recorded and averaged (4–6 stimulations every 30–40 s) before, during, and after unilateral whisker stimulation (20 s at 8–10 Hz). Stimulus-evoked blood flow was expressed as percent change relative to baseline. All experiments were completed in less than 20 min, during which time mouse blood pressure, blood gases, and pH were physiologically stable (Tong et al., 2012).

Local field potential recordings. Mice were anaesthetized with ketamine (70 mg/kg, i.p.) and xylazine (14 mg/kg, i.p.) and placed on a heating blanket for maintaining body temperature at 37°C. Two holes were drilled to place the electrodes, one over the cerebellum for the reference electrode and a second one over the barrel cortex for the recording electrode (Tungsten microelectrodes; FHC). The whisker pad was stimulated electrically by introducing two electrodes into the whisker pad. A stimulator (multichannel system) was used to create a stimulus with the following parameters: 25 consecutive bipolar pulses (0.75 mA, 1 ms duration, 5 Hz). These parameters led to a reproducible blood flow response in the contralateral barrel cortex. Local field potentials were recorded with an amplifier (2 channels Amplifier Model 1800; AM-Systems) and converted into a digital format by an analogue-digital converter (PowerLab 8/30 ML870; ADInstruments). The software LabChart 7 was used to record and to analyze the data (ADInstruments; sampling rate 20 kHz; notch filter 50 Hz). For each mouse, four to six different areas in the barrel cortex were recorded to find the region with the highest response upon whisker stimulation. Each region was stimulated three times with the stimulation protocol described above. The amplitudes of 30 pulses of the region with the highest amplitude were averaged for each mouse.

Pupillary reactivity. We measured pupillary reactivity in awake mice. Eyes were video recorded with a camera (MV830; Canon), which is sensitive in the dark, starting with an illumination of 1 lux. After taking the baseline pupillary diameter for some seconds, a lamp was switched on to increase the illumination to 500 lux. Again, pupils were video-recorded for some seconds to determine minimal pupillary diameter. Diameter was measured manually, each mouse was tested twice and values were averaged.

Behavioral tests. The contextual fear conditioning experiment was performed as described previously (Van der Jeugd et al., 2011). The test chamber (26 × 22 × 18 cm high) was made of clear Plexiglas, and the grid floor was used to deliver an electric shock using a constant current shocker (MED Associates). The test chamber was placed inside a sound attenuated chamber. The experimental period comprised 3 d. On the first day, animals were placed in the testing chamber and were allowed to acclimate for 5 min. On the second day, animals were again placed in the testing chamber and after 2 min of exploration (baseline score), a buzzer was sounded for 30 s. This auditory stimulus, the conditional stimulus, was followed by a 2-s foot shock (0.3 mA), the unconditional stimulus. After the shock, mice were allowed to explore the chamber once more for 1 min before they received a second conditional–unconditional stimulus pairing. Finally, they were allowed to explore for another min. Twenty-four h later, on the third and last day, the animals were placed in the same context for 5 min exploration (context score). After 90 min, the mouse was again placed in the test chamber. Environmental and contextual cues were changed: a white paper square insert was placed in the chamber to alter its color, and mint extract was used to alter the smell. After 3 min of free exploration (preconditional stimulus score), the auditory stimulus was delivered for 3 min (conditional stimulus score). Freezing behavior was recorded every 10 s during each trial block using the standard interval sampling procedure.

Sociability was assessed as described previously (Naert et al., 2013). The setup was made of transparent plexiglass and consisted of a central chamber (42 × 26 cm) that gave access to a left and right chamber (26 × 26 cm) via sliding doors. The left and right chambers contained cylindrical wire cups (10 cm diameter and 11 cm high) in which stranger mice may be present (see below). Two cameras mounted above the setup transferred images to a PC with ANY-mazeVideo Tracking System software (Stoelting). Testing comprised two trials: acclimation trial and sociability trial. During acclimation, the test mouse was placed in the central compartment for 5 min. Divider doors were closed so that the mouse did not have access to the left or right chamber. During the sociability trial, a stranger mouse was placed into the wire cup in either the left or right chamber. Divider doors were opened and the test mouse could freely explore all three chambers. After a 10-min observation period, the test mouse was gently guided toward the central compartment and the divider doors were closed again. Preferential exploration of the stranger mouse over the empty cup was recorded and analyzed. Approaching and spending time within 3 cm of the cup were used to measure exploratory behavior. Stranger mice were female C57BL/6J mice that were group-housed and that had served as stranger mice in other sociability experiments.

Anxiety-related exploration was measured in an elevated plus maze, which mice could freely explore for 10 min. The arena consisted of a plus-shaped maze with two arms (5 cm wide) closed by side walls and two arms without walls. Four IR beams recording open and closed arm entries and one recording the percentage of time per min spent in the open arms were connected to a computerized activity logger. Overall activity was expressed as total counts of entries.

For open field recordings, mice were placed in an illuminated square arena (47 × 47 cm, 160 lux) and video-recorded for 10 min at the indicated time points after tamoxifen injection. Mice were measured during their activity phase (dark phase). Inner zone was centered and defined as 36% of the overall area. The software ANY-maze was used to analyze the percentage of time spent in the inner zone representing a parameter related to anxiety.

Statistical analysis. Based on data from previous projects or from preliminary experiments, we calculated the sample size for key experiments to ensure adequate power to detect prespecified effect sizes. All values are expressed as means ± SEM. Differences were considered to be significant at $P < 0.05$. If distribution was not normal (Kolmogorov-Smirnov test in Prism [GraphPad]), we used either the nonparametric Mann-Whitney or Kruskal-Wallis test. In other cases, we used the two-sided Student's *t* test or ANOVA as indicated in the figure legends. Post-hoc tests were only performed if the ANOVA or Kruskal-Wallis test showed a significant difference. For statistical analysis of MRI data, measurements from the left and right hemispheres were combined for the ROI analysis to maximize statistical power.

We thank Cornelia Magnussen and Gudrun Vierke (Lübeck, Germany); Nadine Gehrig (Heidelberg, Germany); Leen Van Aerschot and Nele De Ruyck (Leuven, Germany); Claudia Brandt, Edith Kaczmarek, and Friederike Twele (Hannover, Germany); as well as Gabriele Frommer-Kästle (Tübingen, Germany), for expert technical assistance; Dr. Jochen Ohnmacht (Lübeck, Germany) for help with the biotin angiography, Dr. Clotilde Leblond-Lecrux (Montréal, Canada) for help with the LFP recordings; Dr. Shizuo Akira (Osaka, Japan) for providing *Tak1*^{Fl} mice; Prof. Wolfgang Bäumgärtner and co-workers (Hannover, Germany) for post mortem examinations of the mice; and Dr. David Shealy (Janssen R&D, Spring House, Pennsylvania) for providing anti-TNF antibodies.

The research leading to these results received funding from the Deutsche Forschungsgemeinschaft to M. Schwaninger (SCHW 413/5-2), and to W. Löscher and K. Töllner (Lo 274/11-2); the internal funding scheme of the University of Lübeck to D.A. Ridder and J. Wenzel; and a joint program of the Canadian Stroke Network and the European Stroke Network (European Union's Seventh Framework Program FP7/2007–2013 under grant agreements 201024 and 202213) to M. Schwaninger, E. Hamel, and L.M. Sorokin. D. Balschun and R. D'Hooge were supported by interdisciplinary research grants from KU Leuven (IDO/06/004 and GOA 12/008).

The authors declare no competing financial interests.

Submitted: 28 January 2015
Accepted: 7 August 2015

REFERENCES

Abe, S., A. Okumura, S. Hamano, M. Tanaka, T. Shiihara, K. Aizaki, T. Tsuru, Y. Toribe, H. Arai, and T. Shimizu. 2011. Early infantile manifestations of incontinentia pigmenti mimicking acute encephalopathy. *Brain Dev.* 33:28–34. http://dx.doi.org/10.1016/j.braindev.2010.04.002

Alvarez, J.I., T. Katayama, and A. Prat. 2013. Glial influence on the blood brain barrier. *Glia*. 61:1939–1958. http://dx.doi.org/10.1002/glia.22575

Argaw, A.T., Y. Zhang, B.J. Snyder, M.L. Zhao, N. Kopp, S.C. Lee, C.S. Raine, C.F. Brosnan, and G.R. John. 2006. IL-1beta regulates blood-brain barrier permeability via reactivation of the hypoxia-angiogenesis program. *J. Immunol.* 177:5574–5584. http://dx.doi.org/10.4049/jimmunol.177.8.5574

Avrahami, E., S. Harel, U. Jurgenson, and D.F. Cohn. 1985. Computed tomographic demonstration of brain changes in incontinentia pigmenti. *Am. J. Dis. Child.* 139:372–374.

Bachevalier, F., C. Marchal, M.P. Di Cesare, A. Antunes, and F. Truchetet. 2003. Atteinte neurologique létale au cours d'une incontinentia pigmenti. *Ann. Dermatol. Venereol.* 130:1139–1142.

Bangerter, N.K., B.A. Hargreaves, S.S. Vasanawala, J.M. Pauly, G.E. Gold, and D.G. Nishimura. 2004. Analysis of multiple-acquisition SSFP. *Magn. Reson. Med.* 51:1038–1047. http://dx.doi.org/10.1002/mrm.20052

Beard, R.S. Jr., R.J. Haines, K.Y. Wu, J.J. Reynolds, S.M. Davis, J.E. Elliott, N.L. Malinin, V. Chatterjee, B.J. Cha, M.H. Wu, and S.Y. Yuan. 2014. Non-muscle Mlck is required for β-catenin- and FoxO1-dependent downregulation of Cldn5 in IL-1β-mediated barrier dysfunction in brain endothelial cells. *J. Cell Sci.* 127:1840–1853. http://dx.doi.org/10.1242/jcs.144550

Bell, R.D., E.A. Winkler, I. Singh, A.P. Sagare, R. Deane, Z. Wu, D.M. Holtzman, C. Betsholtz, A. Armulik, J. Sallstrom, et al. 2012. Apolipoprotein E controls cerebrovascular integrity via cyclophilin A. *Nature*. 485:512–516. http://dx.doi.org/10.1038/nature11087

Boulanger, L.M. 2009. Immune proteins in brain development and synaptic plasticity. *Neuron*. 64:93–109. http://dx.doi.org/10.1016/j.neuron.2009.09.001

Brown, W.R. 2010. A review of string vessels or collapsed, empty basement membrane tubes. *J. Alzheimers Dis.* 21:725–739. http://dx.doi.org/10.3233/JAD-2010-100219

Carman, A.J., J.H. Mills, A. Krenz, D.G. Kim, and M.S. Bynoe. 2011. Adenosine receptor signaling modulates permeability of the blood-brain barrier. *J. Neurosci.* 31:13272–13280. http://dx.doi.org/10.1523/JNEUROSCI.3337-11.2011

Catrysse, L., L. Vereecke, R. Beyaert, and G. van Loo. 2014. A20 in inflammation and autoimmunity. *Trends Immunol.* 35:22–31. http://dx.doi.org/10.1016/j.it.2013.10.005

Chatkupt, S., A.O. Gozo, L.J. Wolansky, and S. Sun. 1993. Characteristic MR findings in a neonate with incontinentia pigmenti. *AJR Am. J. Roentgenol.* 160:372–374. http://dx.doi.org/10.2214/ajr.160.2.8424354

Chen, Y.H., M. Chang, and B.L. Davidson. 2009. Molecular signatures of disease brain endothelia provide new sites for CNS-directed enzyme therapy. *Nat. Med.* 15:1215–1218. http://dx.doi.org/10.1038/nm.2025

Clark, K., S. Nanda, and P. Cohen. 2013. Molecular control of the NEMO family of ubiquitin-binding proteins. *Nat. Rev. Mol. Cell Biol.* 14:673–685. http://dx.doi.org/10.1038/nrm3644

Collins, D.L., P. Neelin, T.M. Peters, and A.C. Evans. 1994. Automatic 3D intersubject registration of MR volumetric data in standardized Talairach space. *J. Comput. Assist. Tomogr.* 18:192–205. http://dx.doi.org/10.1097/00004728-199403000-00005

Cummins, P.M. 2012. Occludin: one protein, many forms. *Mol. Cell. Biol.* 32:242–250. http://dx.doi.org/10.1128/MCB.06029-11

De Lorenzi, R., R. Gareus, S. Fengler, and M. Pasparakis. 2009. GFP-p65 knock-in mice as a tool to study NF-kappaB dynamics in vivo. *Genesis*. 47:323–329. http://dx.doi.org/10.1002/dvg.20468

Dondelinger, Y., M.A. Aguileta, V. Goossens, C. Dubuisson, S. Grootjans, E. Dejardin, P. Vandenabeele, and M.J. Bertrand. 2013. RIPK3 contributes to TNFR1-mediated RIPK1 kinase-dependent apoptosis in conditions of cIAP1/2 depletion or TAK1 kinase inhibition. *Cell Death Differ.* 20:1381–1392. http://dx.doi.org/10.1038/cdd.2013.94

Erickson, M.A., and W.A. Banks. 2013. Blood-brain barrier dysfunction as a cause and consequence of Alzheimer's disease. *J. Cereb. Blood Flow Metab.* 33:1500–1513. http://dx.doi.org/10.1038/jcbfm.2013.135

Everett, R.S., M.K. Vanhook, N. Barozzi, I. Toth, and L.G. Johnson. 2006. Specific modulation of airway epithelial tight junctions by apical application of an occludin peptide. *Mol. Pharmacol.* 69:492–500. http://dx.doi.org/10.1124/mol.105.017251

Fonov, V., A.C. Evans, K. Botteron, C.R. Almli, R.C. McKinstry, and D.L. Collins. Brain Development Cooperative Group. 2011. Unbiased average age-appropriate atlases for pediatric studies. *Neuroimage*. 54:313–327. http://dx.doi.org/10.1016/j.neuroimage.2010.07.033

Gareus, R., E. Kotsaki, S. Xanthoulea, I. van der Made, M.J.J. Gijbels, R. Kardakaris, A. Polykratis, G. Kollias, M.P.J. de Winther, and M. Pasparakis. 2008. Endothelial cell-specific NF-kappaB inhibition protects mice from atherosclerosis. *Cell Metab.* 8:372–383. http://dx.doi.org/10.1016/j.cmet.2008.08.016

Girouard, H., and C. Iadecola. 2006. Neurovascular coupling in the normal brain and in hypertension, stroke, and Alzheimer disease. *J. Appl. Physiol.* 100:328–335. http://dx.doi.org/10.1152/japplphysiol.00966.2005

Goldberg, M.F.M.D. 2004. The skin is not the predominant problem in incontinentia pigmenti. *Arch. Dermatol.* 140:748–750. http://dx.doi.org/10.1001/archderm.140.6.748

Goldmann, T., P. Wieghofer, P.F. Müller, Y. Wolf, D. Varol, S. Yona, S.M. Brendecke, K. Kierdorf, O. Staszewski, M. Datta, et al. 2013. A new type of microglia gene targeting shows TAK1 to be pivotal in CNS autoimmune inflammation. *Nat. Neurosci.* 16:1618–1626. http://dx.doi.org/10.1038/nn.3531

Grand'maison, M., S.P. Zehntner, M.K. Ho, F. Hébert, A. Wood, F. Carbonell, A.P. Zijdenbos, E. Hamel, and B.J. Bedell. 2013. Early cortical thickness changes predict β-amyloid deposition in a mouse model of Alzheimer's disease. *Neurobiol. Dis.* 54:59–67. http://dx.doi.org/10.1016/j.nbd.2013.02.005

Gregor, M.F., and G.S. Hotamisligil. 2011. Inflammatory mechanisms in obesity. *Annu. Rev. Immunol.* 29:415–445. http://dx.doi.org/10.1146/annurev-immunol-031210-101322

Hébert, F., M. Grand'maison, M.K. Ho, J.P. Lerch, E. Hamel, and B.J. Bedell. 2013. Cortical atrophy and hypoperfusion in a transgenic mouse model of Alzheimer's disease. *Neurobiol. Aging*. 34:1644–1652. http://dx.doi.org/10.1016/j.neurobiolaging.2012.11.022

Hennel, S.J., P.G. Ekert, J.J. Volpe, and T.E. Inder. 2003. Insights into the pathogenesis of cerebral lesions in incontinentia pigmenti. *Pediatr. Neurol.* 29:148–150. http://dx.doi.org/10.1016/S0887-8994(03)00150-4

Hirase, T., J.M. Staddon, M. Saitou, Y. Ando-Akatsuka, M. Itoh, M. Furuse, K. Fujimoto, S. Tsukita, and L.L. Rubin. 1997. Occludin as a possible determinant of tight junction permeability in endothelial cells. *J. Cell Sci.* 110:1603–1613.

Ivens, S., D. Kaufer, L.P. Flores, I. Bechmann, D. Zumsteg, O. Tomkins, E. Seiffert, U. Heinemann, and A. Friedman. 2007. TGF-beta receptor-mediated albumin uptake into astrocytes is involved in neocortical epileptogenesis. *Brain*. 130:535–547. http://dx.doi.org/10.1093/brain/awl317

Jacob, A., B. Hack, P. Chen, R.J. Quigg, and J.J. Alexander. 2011. C5a/CD88 signaling alters blood-brain barrier integrity in lupus through nuclear factor-κB. *J. Neurochem.* 119:1041–1051. http://dx.doi.org/10.1111/j.1471-4159.2011.07490.x

Keller, A., A. Westenberger, M.J. Sobrido, M. García-Murias, A. Domingo, R.L. Sears, R.R. Lemos, A. Ordoñez-Ugalde, G. Nicolas, J.E. da Cunha, et al. 2013. Mutations in the gene encoding PDGF-B cause brain calcifications in humans and mice. *Nat. Genet.* 45:1077–1082. http://dx.doi.org/10.1038/ng.2723

Kielland, A., L.M. Camassa, G. Døhlen, L.A. Munthe, R. Blomhoff, M. Amiry-Moghaddam, and H. Carlsen. 2012. NF-κB activity in perinatal brain during infectious and hypoxic-ischemic insults revealed by a reporter mouse. *Brain Pathol.* 22:499–510. http://dx.doi.org/10.1111/j.1750-3639.2011.00548.x

Kisseleva, T., L. Song, M. Vorontchikhina, N. Feirt, J. Kitajewski, and C. Schindler. 2006. NF-kappaB regulation of endothelial cell function during LPS-induced toxemia and cancer. *J. Clin. Invest.* 116:2955–2963. http://dx.doi.org/10.1172/JCI27392

Kolodziej, L.E., J.P. Lodolce, J.E. Chang, J.R. Schneider, W.A. Grimm, S.J. Bartulis, X. Zhu, J.S. Messer, S.F. Murphy, N. Reddy, et al. 2011. TNFAIP3 maintains intestinal barrier function and supports epithelial cell tight junctions. *PLoS ONE*. 6:e26352. http://dx.doi.org/10.1371/journal.pone.0026352

Lau, J.C., J.P. Lerch, J.G. Sled, R.M. Henkelman, A.C. Evans, and B.J. Bedell. 2008. Longitudinal neuroanatomical changes determined by deformation-based morphometry in a mouse model of Alzheimer's disease. *Neuroimage*. 42:19–27. http://dx.doi.org/10.1016/j.neuroimage.2008.04.252

Lomaga, M.A., W.-C. Yeh, I. Sarosi, G.S. Duncan, C. Furlonger, A. Ho, S. Morony, C. Capparelli, G. Van, S. Kaufman, et al. 1999. TRAF6 deficiency results in osteopetrosis and defective interleukin-1, CD40, and LPS signaling. *Genes Dev*. 13:1015–1024. http://dx.doi.org/10.1101/gad.13.8.1015

Madisen, L., T.A. Zwingman, S.M. Sunkin, S.W. Oh, H.A. Zariwala, H. Gu, L.L. Ng, R.D. Palmiter, M.J. Hawrylycz, A.R. Jones, et al. 2010. A robust and high-throughput Cre reporting and characterization system for the whole mouse brain. *Nat. Neurosci*. 13:133–140. http://dx.doi.org/10.1038/nn.2467

Maingay-de Groof, F., M.H. Lequin, D.W. Roofthooft, A.P. Oranje, I.F. de Coo, L.A. Bok, P.J. van der Spek, G.M. Mancini, and P.P. Govaert. 2008. Extensive cerebral infarction in the newborn due to incontinentia pigmenti. *Eur. J. Paediatr. Neurol*. 12:284–289. http://dx.doi.org/10.1016/j.ejpn.2007.09.001

Makris, C., V.L. Godfrey, G. Krähn-Senftleben, T. Takahashi, J.L. Roberts, T. Schwarz, L. Feng, R.S. Johnson, and M. Karin. 2000. Female mice heterozygous for IKK gamma/NEMO deficiencies develop a dermatopathy similar to the human X-linked disorder incontinentia pigmenti. *Mol. Cell*. 5:969–979. http://dx.doi.org/10.1016/S1097-2765(00)80262-2

Matullo, C.M., K.J. O'Regan, H. Hensley, M. Curtis, and G.F. Rall. 2010. Lymphocytic choriomeningitis virus-induced mortality in mice is triggered by edema and brain herniation. *J. Virol*. 84:312–320. http://dx.doi.org/10.1128/JVI.00727-09

Meuwissen, M.E., and G.M. Mancini. 2012. Neurological findings in incontinentia pigmenti; a review. *Eur. J. Med. Genet*. 55:323–331. http://dx.doi.org/10.1016/j.ejmg.2012.04.007

Morioka, S., M. Inagaki, Y. Komatsu, Y. Mishina, K. Matsumoto, and J. Ninomiya-Tsuji. 2012. TAK1 kinase signaling regulates embryonic angiogenesis by modulating endothelial cell survival and migration. *Blood*. 120:3846–3857. http://dx.doi.org/10.1182/blood-2012-03-416198

Naert, A., I. Gantois, A. Laeremans, S. Vreysen, G. Van den Bergh, L. Arckens, Z. Callaerts-Vegh, and R. D'Hooge. 2013. Behavioural alterations relevant to developmental brain disorders in mice with neonatally induced ventral hippocampal lesions. *Brain Res. Bull*. 94:71–81. http://dx.doi.org/10.1016/j.brainresbull.2013.01.008

O'Donnell, M.A., H. Hase, D. Legarda, and A.T. Ting. 2012. NEMO inhibits programmed necrosis in an NFκB-independent manner by restraining RIP1. *PLoS ONE*. 7:e41238. http://dx.doi.org/10.1371/journal.pone.0041238

Obermeier, B., R. Daneman, and R.M. Ransohoff. 2013. Development, maintenance and disruption of the blood-brain barrier. *Nat. Med*. 19:1584–1596. http://dx.doi.org/10.1038/nm.3407

Østergaard, L., S.N. Jespersen, K. Mouridsen, I.K. Mikkelsen, K.Y. Jonsdottír, A. Tietze, J.U. Blicher, R. Aamand, N. Hjort, N.K. Iversen, et al. 2013. The role of the cerebral capillaries in acute ischemic stroke: the extended penumbra model. *J. Cereb. Blood Flow Metab*. 33:635–648. http://dx.doi.org/10.1038/jcbfm.2013.18

Polykratis, A., G. van Loo, S. Xanthoulea, M. Hellmich, and M. Pasparakis. 2012. Conditional targeting of tumor necrosis factor receptor-associated factor 6 reveals opposing functions of Toll-like receptor signaling in endothelial and myeloid cells in a mouse model of atherosclerosis. *Circulation*. 126:1739–1751. http://dx.doi.org/10.1161/CIRCULATIONAHA.112.100339

Ridder, D.A., M.F. Lang, S. Salinin, J.P. Röderer, M. Struss, C. Maser-Gluth, and M. Schwaninger. 2011. TAK1 in brain endothelial cells mediates fever and lethargy. *J. Exp. Med*. 208:2615–2623. http://dx.doi.org/10.1084/jem.20110398

Roy, A., and D.C. Hooper. 2007. Lethal silver-haired bat rabies virus infection can be prevented by opening the blood-brain barrier. *J. Virol*. 81:7993–7998. http://dx.doi.org/10.1128/JVI.00710-07

Saitou, M., M. Furuse, H. Sasaki, J.D. Schulzke, M. Fromm, H. Takano, T. Noda, and S. Tsukita. 2000. Complex phenotype of mice lacking occludin, a component of tight junction strands. *Mol. Biol. Cell*. 11:4131–4142. http://dx.doi.org/10.1091/mbc.11.12.4131

Sakurai, H. 2012. Targeting of TAK1 in inflammatory disorders and cancer. *Trends Pharmacol. Sci*. 33:522–530. http://dx.doi.org/10.1016/j.tips.2012.06.007

Sasaki, Y., E. Derudder, E. Hobeika, R. Pelanda, M. Reth, K. Rajewsky, and M. Schmidt-Supprian. 2006. Canonical NF-kappaB activity, dispensable for B cell development, replaces BAFF-receptor signals and promotes B cell proliferation upon activation. *Immunity*. 24:729–739. http://dx.doi.org/10.1016/j.immuni.2006.04.005

Sato, S., H. Sanjo, K. Takeda, J. Ninomiya-Tsuji, M. Yamamoto, T. Kawai, K. Matsumoto, O. Takeuchi, and S. Akira. 2005. Essential function for the kinase TAK1 in innate and adaptive immune responses. *Nat. Immunol*. 6:1087–1095. http://dx.doi.org/10.1038/ni1255

Schmidt-Supprian, M., W. Bloch, G. Courtois, K. Addicks, A. Israël, K. Rajewsky, and M. Pasparakis. 2000. NEMO/IKK gamma-deficient mice model incontinentia pigmenti. *Mol. Cell*. 5:981–992. http://dx.doi.org/10.1016/S1097-2765(00)80263-4

Schoch, H.J., S. Fischer, and H.H. Marti. 2002. Hypoxia-induced vascular endothelial growth factor expression causes vascular leakage in the brain. *Brain*. 125:2549–2557. http://dx.doi.org/10.1093/brain/awf257

Schwenk, F., U. Baron, and K. Rajewsky. 1995. A cre-transgenic mouse strain for the ubiquitous deletion of loxP-flanked gene segments including deletion in germ cells. *Nucleic Acids Res*. 23:5080–5081. http://dx.doi.org/10.1093/nar/23.24.5080

Seiffert, E., J.P. Dreier, S. Ivens, I. Bechmann, O. Tomkins, U. Heinemann, and A. Friedman. 2004. Lasting blood-brain barrier disruption induces epileptic focus in the rat somatosensory cortex. *J. Neurosci*. 24:7829–7836. http://dx.doi.org/10.1523/JNEUROSCI.1751-04.2004

Sled, J.G., A.P. Zijdenbos, and A.C. Evans. 1998. A nonparametric method for automatic correction of intensity nonuniformity in MRI data. *IEEE Trans. Med. Imaging*. 17:87–97. http://dx.doi.org/10.1109/42.668698

Sonkusare, S.K., A.D. Bonev, J. Ledoux, W. Liedtke, M.I. Kotlikoff, T.J. Heppner, D.C. Hill-Eubanks, and M.T. Nelson. 2012. Elementary Ca2+ signals through endothelial TRPV4 channels regulate vascular function. *Science*. 336:597–601. http://dx.doi.org/10.1126/science.1216283

Sorokin, L.M., F. Pausch, M. Frieser, S. Kröger, E. Ohage, and R. Deutzmann. 1997. Developmental regulation of the laminin alpha5 chain suggests a role in epithelial and endothelial cell maturation. *Dev. Biol*. 189:285–300. http://dx.doi.org/10.1006/dbio.1997.8668

Taccone, F.S., F. Su, C. Pierrakos, X. He, S. James, O. Dewitte, J.L. Vincent, and D. De Backer. 2010. Cerebral microcirculation is impaired during sepsis: an experimental study. *Crit. Care*. 14:R140. http://dx.doi.org/10.1186/cc9205

Tong, X.K., N. Nicolakakis, A. Kocharyan, and E. Hamel. 2005. Vascular remodeling versus amyloid beta-induced oxidative stress in the cerebrovascular dysfunctions associated with Alzheimer's disease. *J. Neurosci*. 25:11165–11174. http://dx.doi.org/10.1523/JNEUROSCI.4031-05.2005

Tong, X.K., N. Nicolakakis, P. Fernandes, B. Ongali, J. Brouillette, R. Quirion, and E. Hamel. 2009. Simvastatin improves cerebrovascular function and counters soluble amyloid-beta, inflammation and oxidative stress in aged APP mice. *Neurobiol. Dis*. 35:406–414. http://dx.doi.org/10.1016/j.nbd.2009.06.003

Tong, X.K., C. Lecrux, P. Rosa-Neto, and E. Hamel. 2012. Age-dependent rescue by simvastatin of Alzheimer's disease cerebrovascular and memory deficits. *J. Neurosci*. 32:4705–4715. http://dx.doi.org/10.1523/JNEUROSCI.0169-12.2012

Tripathi, A.K., W. Sha, V. Shulaev, M.F. Stins, and D.J. Sullivan Jr. 2009. Plasmodium falciparum-infected erythrocytes induce NF-kappaB regulated inflammatory pathways in human cerebral endothelium. *Blood*. 114:4243–4252. http://dx.doi.org/10.1182/blood-2009-06-226415

Tronche, F., C. Kellendonk, O. Kretz, P. Gass, K. Anlag, P.C. Orban, R. Bock, R. Klein, and G. Schütz. 1999. Disruption of the glucocorticoid receptor gene in the nervous system results in reduced anxiety. *Nat. Genet.* 23:99–103. http://dx.doi.org/10.1038/12703

Tsao, N., H.P. Hsu, C.M. Wu, C.C. Liu, and H.Y. Lei. 2001. Tumour necrosis factor-alpha causes an increase in blood-brain barrier permeability during sepsis. *J. Med. Microbiol.* 50:812–821.

Van der Jeugd, A., T. Ahmed, S. Burnouf, K. Belarbi, M. Hamdame, M.-E. Grosjean, S. Humez, D. Balschun, D. Blum, L. Buée, and R. D'Hooge. 2011. Hippocampal tauopathy in tau transgenic mice coincides with impaired hippocampus-dependent learning and memory, and attenuated late-phase long-term depression of synaptic transmission. *Neurobiol. Learn. Mem.* 95:296–304. http://dx.doi.org/10.1016/j.nlm.2010.12.005

van Loo, G., R. De Lorenzi, H. Schmidt, M. Huth, A. Mildner, M. Schmidt-Supprian, H. Lassmann, M.R. Prinz, and M. Pasparakis. 2006. Inhibition of transcription factor NF-kappaB in the central nervous system ameliorates autoimmune encephalomyelitis in mice. *Nat. Immunol.* 7:954–961. http://dx.doi.org/10.1038/ni1372

Vanlangenakker, N., T. Vanden Berghe, P. Bogaert, B. Laukens, K. Zobel, K. Deshayes, D. Vucic, S. Fulda, P. Vandenabeele, and M.J. Bertrand. 2011. cIAP1 and TAK1 protect cells from TNF-induced necrosis by preventing RIP1/RIP3-dependent reactive oxygen species production. *Cell Death Differ.* 18:656–665. http://dx.doi.org/10.1038/cdd.2010.138

Wu, C., F. Ivars, P. Anderson, R. Hallmann, D. Vestweber, P. Nilsson, H. Robenek, K. Tryggvason, J. Song, E. Korpos, et al. 2009. Endothelial basement membrane laminin alpha5 selectively inhibits T lymphocyte extravasation into the brain. *Nat. Med.* 15:519–527. http://dx.doi.org/10.1038/nm.1957

Xiao, Y., H. Li, J. Zhang, A. Volk, S. Zhang, W. Wei, S. Zhang, P. Breslin, and J. Zhang. 2011. TNF-α/Fas-RIP-1-induced cell death signaling separates murine hematopoietic stem cells/progenitors into 2 distinct populations. *Blood.* 118:6057–6067. http://dx.doi.org/10.1182/blood-2011-06-359448

Ye, X., J. Ding, X. Zhou, G. Chen, and S.F. Liu. 2008. Divergent roles of endothelial NF-kappaB in multiple organ injury and bacterial clearance in mouse models of sepsis. *J. Exp. Med.* 205:1303–1315. http://dx.doi.org/10.1084/jem.20071393

Zhang, X., J.A. Winkles, M.C. Gongora, R. Polavarapu, J.S. Michaelson, K. Hahm, L. Burkly, M. Friedman, X.J. Li, and M. Yepes. 2007. TWEAK-Fn14 pathway inhibition protects the integrity of the neurovascular unit during cerebral ischemia. *J. Cereb. Blood Flow Metab.* 27:534–544. http://dx.doi.org/10.1038/sj.jcbfm.9600368

Zhang, L., P. Papadopoulos, and E. Hamel. 2013. Endothelial TRPV4 channels mediate dilation of cerebral arteries: impairment and recovery in cerebrovascular pathologies related to Alzheimer's disease. *Br. J. Pharmacol.* 170:661–670. http://dx.doi.org/10.1111/bph.12315

Zhu, W., N.R. London, C.C. Gibson, C.T. Davis, Z. Tong, L.K. Sorensen, D.S. Shi, J. Guo, M.C. Smith, A.H. Grossmann, et al. 2012. Interleukin receptor activates a MYD88-ARNO-ARF6 cascade to disrupt vascular stability. *Nature.* 492:252–255. http://dx.doi.org/10.1038/nature11603

Zlokovic, B.V. 2008. The blood-brain barrier in health and chronic neurodegenerative disorders. *Neuron.* 57:178–201. http://dx.doi.org/10.1016/j.neuron.2008.01.003

Zlokovic, B.V. 2011. Neurovascular pathways to neurodegeneration in Alzheimer's disease and other disorders. *Nat. Rev. Neurosci.* 12:723–738. http://dx.doi.org/10.1038/nrn3114